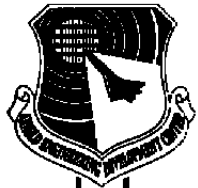# Computation of Inlet Reference Plane Flow-Field for a Subscale Free-Jet Forebody/Inlet Model and Comparison to Experimental Data

M. D. McClure and J. R. Sirbaugh
Sverdrup Technology, Inc.

February 1991

Final Report for Period January 1, 1989 to July 31, 1990

Approved for public release; distribution is unlimited.

**ARNOLD ENGINEERING DEVELOPMENT CENTER
ARNOLD AIR FORCE BASE, TENNESSEE
AIR FORCE SYSTEMS COMMAND
UNITED STATES AIR FORCE**

This report has been reviewed by the Office of Public Affairs (PA) and is releasable to the National Technical Information Service (NTIS). At NTIS, it will be available to the general public, including foreign nations.

APPROVAL STATEMENT

This report has been reviewed and approved.

MARJORIE S. COLLIER
Directorate of Technology
Deputy for Operations

Approved for publication:

FOR THE COMMANDER

KEITH L. KUSHMAN
Technical Director
Directorate of Technology
Deputy for Operations

REPORT DOCUMENTATION PAGE

1 AGENCY USE ONLY (Leave blank)	2 REPORT DATE **February 1991**	3. REPORT TYPE AND DATES COVERED **Final January 1, 1989 to July 31, 1990**

4 TITLE AND SUBTITLE **Computation of Inlet Reference Plane Flow Field for a Subscale Free-Jet Forebody/Inlet Model and Comparison to Experimental Data**	5 FUNDING NUMBERS **PE 65807F**
6 AUTHOR(S) . **McClure, M. D. and Sirbaugh, J. R., Sverdrup Technology, Inc., AEDC Group**	

7 PERFORMING ORGANIZATION NAME(S) AND ADDRESS(ES) **Arnold Engineering Development Center/DOT Air Force Systems Command Arnold Air Force Base, TN 37389-5000**	8 PERFORMING ORGANIZATION REPORT NUMBER **AEDC-TR-90-21**

9 SPONSORING/MONITORING AGENCY NAMES(S) AND ADDRESS(ES) **Arnold Engineering Development Center/DO Air Force Systems Command Arnold Air Force Base, TN 37389-5000**	10. SPONSORING/MONITORING AGENCY REPORT NUMBER

11 SUPPLEMENTARY NOTES
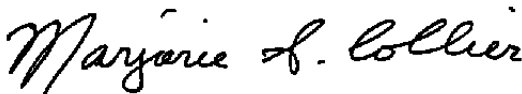
Available in Defense Technical Information Center (DTIC).

12a DISTRIBUTION/AVAILABILITY STATEMENT **Approved for public release; distribution is unlimited.**	12b DISTRIBUTION CODE

13 ABSTRACT (Maximum 200 words)

The computational fluid dynamics (CFD) computer code PARC3D was used to predict the inlet reference plane (IRP) flow field for a side-mounted inlet and forebody simulator in a free jet for five different flow conditions. The calculations were performed for free-jet conditions, mass flow rates, and inlet configurations that matched the free-jet test conditions. In addition, viscous terms were included in the main flow so that the viscous free-jet shear layers emanating from the free-jet nozzle exit were modeled. A measure of the predicted accuracy was determined as a function of free-stream Mach number, angle-of-attack, and sideslip angle.

14. SUBJECT TERMS free jet forebody simulator inlet reference plane			15 NUMBER OF PAGES **78**
			16 PRICE CODE

17 SECURITY CLASSIFICATION OF REPORT **UNCLASSIFIED**	18 SECURITY CLASSIFICATION OF THIS PAGE **UNCLASSIFIED**	19 SECURITY CLASSIFICATION OF ABSTRACT **UNCLASSIFIED**	20. LIMITATION OF ABSTRACT **SAME AS REPORT**

PREFACE

CONTENTS

ILLUSTRATIONS

TABLES

1.0 INTRODUCTION

1.1 BACKGROUND

Aircraft designs rely on properly integrated propulsion system components (i.e. engines, inlets, and airframes) to produce optimum overall performance. Because of the complexity of designing such a system, the integrated components need to be thoroughly tested prior to finalizing the full-scale aircraft design. However, many full-scale propulsion systems are too large for even the largest ground test facilities. Therefore, either full-scale components are tested separately, or only subscale models are tested with engine simulators. If components are tested separately, performance of the integrated system is often difficult to predict. For example, when an engine is tested using the direct-connect technique, the airframe and inlet influence on the engine face airflow must be approximated by some means such as distortion screens or airjet distortion generators. The arrangement of distortion screens is determined based on either the inlet manufacturer's performance information or results from subscale testing. Although an excellent evaluation of engine performance may be obtained, the engine/inlet and airframe interaction may not be accurately evaluated. The alternative to testing components separately is subscale testing of airframe and inlet models using engine simulators.

1.2 REQUIREMENTS

Important to the design of fighter aircraft is engine/inlet performance, particularly when the airframe is at large angles of pitch and/or yaw. The free-jet test technique under development for use in the Arnold Engineering Development Center (AEDC) Aeropropulsion Systems Test Facility (ASTF) permits full-scale engines to be tested in conjunction with actual inlets and forebodies or forebody simulators (Ref. 1). A forebody simulator (FBS) is generally required because the actual forebody is too large for even the largest test facilities. The FBS must be designed to generate a flow field at the inlet that closely approximates the aircraft forebody effects in flight. This test technique will permit realistic engine/inlet compatibility data to be obtained over a range of attitude angles because engine face distortion is properly generated by the inlet and forebody simulator (Ref. 2).

In a free-jet test, the engine, inlet, and forebody simulator are positioned in a test cell while a jet of air at appropriate test conditions is blown over the integrated components. The jet can be introduced at various incidences to simulate angle-of-attack and sideslip effects. The intended result is to create, in the confined space of a test cell, a flow field in the immediate vicinity of the inlet that is representative of the total aircraft in free flight. This plane where free-flight conditions are matched will be referred to, herein, as the inlet reference plane (IRP). If correct flow conditions are provided at the IRP, it is assumed that the engine/inlet system

is presented with a flow field that is representative of the aircraft in free flight. This can be achieved by closely monitoring the IRP flow field and adjusting the jet to produce the desired flow field. Two fundamental questions that must be answered in order to make the free-jet testing concept a viable method of testing integrated propulsion systems are (1) how to define the desired or target IRP flow field and (2) how to design forebody simulators.

The IRP flow field must be known in advance to perform free-jet testing. The flow field can be determined by subscale testing using an engine simulator and/or by a nontesting technique such as computational fluid dynamics (CFD), as discussed in Ref. 2. Subscale testing produces accurate flow-field characteristics, such as shock waves, boundary layers, and separated flows if reasonable care is taken with respect to model geometry and Reynolds number scaling. The main disadvantage of subscale testing is the time and cost associated with building and testing the model. On the other hand, CFD solutions potentially require less time and cost than subscale testing if an appropriate and adequately validated computer code is available.

For a CFD code to be used in determining the target IRP flow field, the code must have been proven to have adequate flow-field prediction accuracy. Adequate prediction accuracy implies that the predicted IRP flow field is the same as the actual flow field to within an acceptable tolerance. The tolerance limits may vary depending on the test article, test objectives, and test conditions.

Forebody simulators must be designed to replace the actual forebody, if too large to fit into existing engine test cells, before free-jet testing can be performed. Only two obvious means to design forebody simulators are available, subscale cut-and-try testing and CFD. Subscale testing consists of taking slices of the full forebody as the basis for model configurations that are tested until sufficient agreement between target IRP conditions and measured IRP conditions are obtained. This approach was used to design forebody simulators for full-scale F-15 inlet-engine tests. The same procedure has been followed in conjunction with CFD; however recent development work at AEDC, indicates that an optimization method may be used in conjunction with CFD to more efficiently design forebody simulators (Ref. 3). Both computational trial-and-error and optimization require that a prediction tool of sufficient accuracy be available to support the work. The level of accuracy of the prediction tool is subjective and depends on such variables as test article, test objectives, and test conditions as stated previously.

1.3 OBJECTIVE

A series of free-jet tests were conducted as part of current AEDC free-jet test technique studies in which the IRP flow fields for a subscale side-mounted inlet and forebody

configuration, including an engine simulator, were measured. The PARC3D CFD code was then used to simulate selected free-jet test points. The objective of this work was to determine the degree of accuracy with which the PARC3D code could predict these experimentally determined conditions and, thus, the capability of CFD as a design tool to converge on the optimum forebody simulator for a given IRP flow field.

This report describes the free-jet tests, discusses the measurements obtained including data quality, reviews aspects of the CFD code utilized, presents comparisons of measured and computed IRP flow fields, and based on these comparisons, makes observations relevant to the use of the PARC3D CFD code for supporting free-jet testing.

2.0 FREE-JET TEST PROGRAM

A multiphase experimental test program is underway in the AEDC pilot free-jet test facility (R2A2). The primary purpose of the test program is to validate the overall free-jet test technique and to aid in the design and use of the ASTF C2 free-jet facility. Validation of the free-jet test technique is performed by reproducing IRP conditions obtained in a supporting wind tunnel test program and then evaluating inlet distortion comparisons relative to established validation criteria (Ref. 4). An additional test objective is to generate a CFD code comparison database.

The test article consists of a 1/6-scale F-15 inlet model with four different forebody simulators. Free-jet test conditions referenced in this report are the corresponding match points from the wind tunnel test program and not the free-jet nozzle settings used in the free-jet test program. Tests were conducted at subsonic Mach numbers of 0.3, 0.6, and 0.9 for angles-of-attack, ALPHA, from − 10 to 35 deg and angles-of-sideslip, BETA, of − 10 to 10 deg. Tests were also conducted at a supersonic Mach number of 2.2 for ALPHA values of − 5 to 15 deg and BETA values from − 6 to 6 deg. Three different inlet mass flow rates were used at both subsonic and supersonic Mach numbers. The specific test conditions to be applied to each forebody simulator are shown in Tables 1 and 2. The free-jet test results obtained between October 1987 and December 1989 were used in the comparisons reported herein.

The model included a fully functional inlet with variable geometry features. The inlet cowl was movable and driven by an external drive. A driven four-ramp system modeled the internal mechanism of the actual F-15 aircraft inlet. The inlet internal geometry extended aft to a simulated engine face. The inlet mass flow was controlled by a remotely actuated flow-control plug located aft of the simulated engine face. During supersonic testing, a bleed duct between the third and fourth ramps was used to maintain subsonic flow at the inlet throat. A representative boundary-layer diverter ramp was placed between the inlet and forebody simulator. The model as installed in R2A2 is shown in Fig. 1.

Forebody simulators used in the study were fabricated at AEDC. Forebody Simulators 1 and 2 (FBS1 and FBS2) are short slices of the full F-15 forebody with the same inlet side contours. Forebody Simulators 3 and 4 (FBS3 and FBS4) were designed by trial-and-error using CFD-generated streamline traces to aid in the length selection. FBS3 was an attempt to provide forebody effect over a wide range of Mach numbers and flight attitudes, whereas FBS4 was a point design optimized for operation at Mach number 0.9, ALPHA of 30.0, and BETA of 10.

Detailed drawings and/or geometry coordinates of the inlet sidewalls and diverter ramp were not available for use in this study; therefore, coordinates for model components were obtained from various sources, including examination of the model. It is believed that the geometry of these components was determined to a sufficient degree of accuracy for this study.

Data were obtained using calibrated combination Mach/flow angularity probes at the IRP, total pressure probes at the simulated engine face, and static pressure taps located on the four ramps and on the floor of the inlet. The IRP was parallel to and 3.1 in. from the inlet face when the cowl was undeflected (Fig. 2a). Three cone probes (Fig. 2b) formed the IRP rake assembly (Fig. 2c). This assembly was mounted on a remotely actuated traverse mechanism located below the inlet. To maintain the cone probes in their calibration range and to more closely align them with the local flow upwash, the rake assembly was mounted at three different offset angles relative to the model. No offset angle variation was provided for sidewash. IRP Mach number (MACHI), and IRP flow angles (ALPHAI and BETAI) were determined as a function of measured probe pressures. Figure 3 graphically defines the flow angles ALPHAI and BETAI. During the course of testing, Probe 3 became inoperable; however, the test program was continued because of cost and resource considerations. The engine face total pressure was measured with eight rakes positioned 45 deg apart. Each rake consisted of five pairs of steady-state and high-response total pressure probes. The inlet throat Mach number was determined using a total pressure probe located just above the floor of the inlet and a static pressure tap located forward of the total pressure probe.

R2A2 is equipped with interchangeable subsonic and supersonic nozzles that permit testing at different Mach numbers and ALPHA and BETA. The nozzles can be rotated to direct the flow of air at the test article from different angles. The test article was also rotated relative to the test cell centerline to create the required combined ALPHA and BETA conditions during subsonic testing. During supersonic testing, the free-jet nozzle sidewalls were rotated about their downstream ends to vary exit Mach numbers.

3.0 IRP RAKE CALIBRATION

The three-probe IRP rake was calibrated in Aerodynamic Wind Tunnel 4T over a range of Mach numbers and attitude angles. Calibration data were taken for a pitch and yaw range of ±27 deg. Measurements were obtained at Mach numbers of 0.3, 0.4, 0.6, 0.8, 0.9, 0.95, 1.05, 1.1, 1.3, 1.6, and 2.0. At all Mach numbers other than 0.8 and 1.3, calibration data were obtained with either pitch or yaw set to zero while varying the other parameter. At Mach numbers 0.8 and 1.3, combined pitch and yaw calibration data were obtained. Calibration curve fits were generated that related the measured cone probe surface pressures to the known tunnel Mach number and rake attitude angles. Although the combined pitch and yaw data were not used to generate the analytic curve fits, these data were used to check these derived curve-fit algorithms' accuracy for combined angles.

4.0 EXPERIMENTAL DATA UNCERTAINTY

An extensive investigation of the Tunnels 16T and 16S IRP data uncertainty was conducted in July 1988. All known uncertainty contributors to the Tunnel 4T IRP rake calibration and the Tunnels 16T and 16S 1/6-scale F-15 tests were included. Estimates of the contributions were made from various published sources, engineering estimates, and the probe calibration test results. All uncertainty contributors were evaluated at various Mach numbers and local probe angles and then combined using the method of Abernethy and Thompson (Ref. 5).

The major uncertainty contributor was found to be the probe calibration curve fit. The curve-fit uncertainty contribution was found to increase as a function of total flow angle relative to the probe. Although curve fits were developed for each of the three probes, the curve fit contribution to the total uncertainty estimate was derived by examining only one of the three probes. The uncertainty findings are summarized in the form of contour plots (Figs. 4, 5, and 6) where the uncertainty of the IRP parameters is shown as a function of flow angles relative to the probes at different Mach number levels.

The maximum total flow angle (relative to the probe) for which the probes were calibrated was 27 deg. Any measured data with a combined angle greater than 27 deg were considered to have an unknown uncertainty. IRP data obtained in the F-15 tests that represent angles of 27 deg relative to the probe have, on the average, an uncertainty of 3 deg. Therefore, the largest reported flow angle relative to the probe that definitely lies within the calibration range is 24 deg; only data with combined angles of 24 deg or less were considered in the CFD comparison. The rake offset angles, which were selected to more closely align the local flow with the probes, were accounted for in determining experimental uncertainty values for measured data.

A word of caution with respect to data uncertainty needs to be mentioned. The uncertainty magnitudes should not be associated with a normal probability distribution because the curve-fit contribution appears as a bias term in the total uncertainty estimates. In the case of the calibration curve-fit contribution, an insufficient amount of independent and/or repeat data were available to establish data uncertainty to a high degree of accuracy. Therefore, the data uncertainty values used herein are estimates based on available information and experience.

5.0 COMPUTATIONS

A fundamental requirement of free-jet testing, that the IRP flow field be matched (within some tolerance) to conditions commensurate with free flight, is achieved by replacing the full forebody with an aerodynamically equivalent forebody simulator and setting appropriate free-jet conditions. In order to satisfy this requirement in the least expensive fashion, CFD is being investigated as a tool to design and certify forebody simulator designs prior to testing. Experience has shown that CFD codes that solve the Euler equations can accurately predict very complex flow fields, as long as viscous effects are not dominant. For forebody/inlet configurations at moderate ALPHA and BETA, it is assumed that the Euler equations are adequate to predict IRP flow fields for many configurations of interest. The free-jet environment, however, consists primarily of an inviscid core flow surrounded by a viscous shear layer. In order to resolve the details of the viscous shear layers, the Navier-Stokes terms including a turbulence model must be included in the code.

The first step in demonstrating a CFD forebody design capability is to demonstrate a CFD free-jet IRP prediction capability. The Euler/Navier-Stokes computer code PARC3D (Ref. 6) was tested for IRP prediction accuracy by simulating five test cases from the previously described experimental test program. CFD modeling considerations included the inlet and forebody simulator geometries, location and types of boundary conditions, grid resolution, treatment of inlet mass flow rates, and description of related test hardware. All solid surfaces were modeled as inviscid slip surfaces. Therefore, forebody and inlet viscous effects were ignored. Viscous terms were included in the main flow so that the viscous free-jet shear layers emanating from the nozzle exit were modeled. Calculations were performed for this effort for free-jet conditions, mass flow rates, and inlet configurations that matched the free-jet test conditions. Computations were performed for the five test cases (Table 3). Version 5.1 of the PARC3D computer code was used in the preceding, and the basic algorithm was not modified during the course of these investigations.

5.1 PARC3D

The PARC3D computer code (Ref. 6) solves the strong conservation law form of the Navier-Stokes and Euler equations. Two solution algorithms are available in PARC3D. The

Beam and Warming approximate factorization scheme is used to form the implicit central-difference algorithm (Ref. 7). The equations are solved using the scalar pentadiagonal transformation developed by Pulliam (Ref. 8). The second algorithm is based on the Jameson explicit finite volume multistage algorithm (Ref. 9). The most unique feature of PARC3D is that the user can specify computational boundary conditions via data input anywhere in the computational domain, thus making PARC3D ideally suited for such complicated geometries as side-mounted inlets.

PARC3D permits two types of domain decomposition or grid blocking. The first type simply allows for decomposing a single grid into subdomains to circumvent in-core computer memory limitations. The communication between subdomains is handled through user-supplied boundary conditions known as contiguous interfaces. The second form of decomposition allows for dissimilar grids overlapping to cover a larger domain. Should the different subdomains overlap in an easily defined fashion, then communication between blocks is again handled through user-supplied boundary conditions referred to as noncontiguous interfaces. However, should the dissimilar grids overlap in a more general fashion, communication between blocks is handled through input data created by a preprocessor, PEGASUS (Ref. 10). This type of subdomain communication is referred to as a Chimera interface. As previously mentioned, the Navier-Stokes option, including a turbulence model, was used to obtain all solutions presented herein.

5.2 CFD MODEL

Subsonic computations were performed using the implicit algorithm and only contiguous subdomain interfaces. The computational domain was modeled with two grids, an inlet grid and a test cell region grid. The inlet grid contained 46,000 grid points and the cell region grid contained 185,000 grid points and modeled part of the free-jet nozzle, test cell, forebody simulator, boundary-layer diverter ramp, inlet internal and external geometries, and IRP traverse mechanism. The free-jet nozzle and test article orientation relative to the test cell were matched to the set experimental conditions. The inlet cowl and internal ramps were positioned as in the free-jet test. The grid was designed to minimize the time required to simulate other test conditions that required repositioning the free-jet nozzle, test article and/or inlet. The grid structure is indicated in Fig. 7, and selected cross sections of the grid are included in Fig. 8.

A portion of the IRP survey rake traverse mechanism was included in the computational model to simulate its effect on the IRP flow-field parameters. The mechanism, as shown installed on the wind tunnel model in Fig. 9, was simulated in the subsonic free-jet calculations at the same relative location. Since the actual mechanism was too complex in shape to fully model computationally, it was approximated by projecting the shape of the most forward

faces of the mechanism onto the exit plane grid and then determining which grid points were enclosed within the mechanism shape. The presence of the mechanism was simulated by specifying these points to lie on a solid flat surface (Fig. 10).

Computational boundary conditions were specified to match test cell conditions and to impose inviscid slip surfaces. For the free-jet calculations, the test cell total pressure and temperature were specified as a "free" boundary condition (Ref. 6) at the inflow plane of the free-jet nozzle. Experimental static cell pressure was imposed as the downstream cell exit plane boundary condition. ALPHA and BETA were imposed by the rotation of the free-jet nozzle, whereas nozzle exit plane Mach number was not imposed but resulted from the upstream total to the downstream static pressure ratio. Solid walls were simulated by setting velocities normal to the wall to zero while maintaining total conditions on the wall equal to conditions just off the wall. Inlet mass flow was simulated by specifying the experimentally measured flow rate at the downstream boundary of the inlet. The mass flux boundary condition used in PARC3D adjusts the local static pressure at the boundary to achieve the proper mass flow rate.

Because of the large number of grid points used for the computations, solutions were obtained by decomposing the global grid into n subdomains. Each subdomain represented the largest grid size that could be run in PARC3D on the AEDC XMP-12 CRAY® computer. Solutions were generated by iterating one time on each grid block and repeating the iteration process until convergence was obtained. Each subdomain overlapped its neighboring subdomains by two grid points. Flow-field information was transferred between subdomains after each iteration.

Supersonic calculations were performed in a similar manner, except the global domain was composed of three major subdomains and the explicit solution algorithm was required. The three major subdomains consisted of the free-jet nozzle and test cell grid, the forebody simulator grid, and the inlet grid. Communication between the major subdomains was accomplished through the use of Chimera-type interfaces. Each major subdomain was also decomposed into several smaller subdomains to maintain compatibility with limited in-core CRAY computer memory. The Chimera-type boundary conditions were employed in the supersonic calculations mainly because the relative location of the forebody simulator and inlet to the free-jet nozzle prevented a single grid topology from modeling all possible free-jet nozzle movements. The explicit solution algorithm was used since the current implementation of the Chimera-type boundary condition restricts the solution algorithm to a three-point solution stencil in some portions of the grid. The implicit algorithm is a five-point stencil.

Boundary conditions for the supersonic cases were the same as the subsonic cases with a few exceptions. The variable throat area capability of the free-jet nozzle was used both in the experiment and in the calculations to set the nozzle exit plane Mach number. The grid-blocking strategy for the supersonic cases is shown in Fig. 11 and selected grid plots are shown in Fig. 12.

5.3 CONVERGENCE

Subsonic calculations were considered converged when the inlet mass flow rate had converged to within 0.1 percent of the desired mass flow. Convergence based on inlet mass flow was determined to be a more sensitive criteria than more conventional criteria. Subsonic cases were typically considered converged after 1,000 iterations, which required 12 hr of the AEDC CRAY XMP-12 central processor time and 8 hr of input/output time. Input/output was to the CRAY DD-29 disk drives. Even in a dedicated computer environment, 18 hr of wall clock time would have been required to compute each case. It should be noted that the actual turnaround time required to obtain each solution was from 3 to 5 days because the AEDC CRAY is a shared resource.

Supersonic calculations were considered converged when the subdomains containing the inlet had reduced the solution residual three orders-of-magnitude from the initial uniform flow fields. Typically 2,500 iterations were required to converge each solution. The increased number of iterations is caused by using the slower converging explicit scheme and the presence of multiple reflected shocks emanating from the leading edge of the forebody simulator and inlet. On the order of 20 hr of central process time and 20 hr of input/output were required for each supersonic case. Turnaround time for each supersonic case averaged 10 days.

6.0 RESULTS

As stated earlier, the original goal of the present effort was to evaluate the ability of PARC3D to predict IRP flow fields associated with forebody/inlet configurations in a free-jet environment. In order to achieve this goal completely, several characteristics should be true of the experimental database and computations. The experimental geometry and procedure followed must be representative of the true geometries to be modeled. The geometry and test conditions should be adequately documented to assure that the computational simulation is representative of the true geometries and test conditions. The experimental data should be of high quality, with known and acceptable uncertainty magnitude.

The F-15 inlet model was an appropriate geometry for this effort; however, the CFD model as tested was not as aerodynamically clean as would be desired, primarily because of skewed grid regions (Figs. 8 and 12). Resource constraints dictated that the CFD model

end downstream of the inlet lower lip, but upstream of the majority of the related test hardware, thus avoiding the complicated hardware and its associated grid complexities. Differences between experimental and computational configurations, such as exclusion of the true probe traverse mechanism geometry from the CFD model, implied that the origin of differences between measured and computed IRP conditions would be difficult (if not impossible) to ascertain for the subsonic cases.

An additional difference between the experimental and computational model was an inlet throat bleed slot opening that was not modeled computationally. The computational mass flow boundary was placed downstream of the throat resulting in an incorrect inlet mass flow being calculated for the supersonic cases. A subsequent study showed that placing the mass flow boundary upstream of the throat allowed the proper mass flow to be captured by the inlet, but did not affect the computed flow properties at the IRP, since the flow is primarily supersonic up to that point.

The experimental data were well understood and of known uncertainty, but resulted in a less than desirable assessment of the code's IRP prediction accuracy. Because of experimental data uncertainty, IRP measurements obtained in the F-15 tests could not be treated as exact flow-field values when experimental results were compared to computational results. Each experimental data value was transformed into an experimental data band, centered at the measured value, with width equal to twice the experimental uncertainty. Also, a normal probability distribution was not associated with the resulting uncertainty band. Neither the actual probability distribution, nor the value of highest probability, was known. Because of the nature of the bias term in the uncertainty estimates, the true value would probably lie on one side or the other of the measured value, especially for cases that have large combined flow angles (which was true of the majority of the experimental data considered).

The experimental uncertainty of an IRP data point was obtained by first converting the measured flow angles from the model-oriented coordinate system to the probe-oriented coordinate system, taking into account the rake mount angle. A screening was then used to discard data points that had a combined flow angle greater than 24 deg. The converted flow angles and reported local Mach number were then used to interpolate uncertainty values from the uncertainty contour plots (Figs. 4, 5, and 6). Uncertainty values at the higher contour level were used for those IRP values between two uncertainty contour levels. The available Mach 2.0 uncertainty data were used to estimate IRP uncertainty values for data with measured MACHI values greater than 2.0. The computed IRP values were obtained by a numerical survey of the predicted flow field. The survey was performed by linearly interpolating the computed gas dynamic variables onto 40 evenly spaced points along each of the three probe paths. The interpolated variables were then used to calculate IRP values of MACHI, ALPHAI, and BETAI. The location of the survey point was assumed to be at the tip of the probe.

The measured and computed IRP plot format is illustrated in Fig. 13. Presented in Figs. 14 through 18 are the comparisons for the five cases in terms of local MACHI, ALPHAI, and BETAI values. These plots facilitate the comparison of predicted and measured IRP data on a probe-by-probe and point-by-point basis. The abscissa indicates the dependent IRP parameter (MACHI, ALPHAI, or BETAI); the ordinate indicates the independent parameter (rake location). The rake location is measured in inches from the aft-most or lowest rake position. Therefore, a rake location of 16 in. is near the leading edge of the inlet, and 3.2 in. is near the cowl lip. The plot subtitle indicates the probe position relative to the fuselage as either INBOARD, which is nearest the fuselage, CENTER, or OUTBOARD, which is farthest from the fuselage. The experimental data, including the uncertainty estimate, are presented as a cross-hatched band. The computational results are represented as a solid line drawn through the 40 interpolated data points with the most forward or highest region of the IRP being at the top and the most aft or lowest region being at the bottom of the plots. The computational curves are marked on each end by a symbol. Computed results for the outboard probe are included in the plots to show trends even though experimental data are not available for comparison.

Comparison plots are grouped so that a single IRP parameter for all three probes is shown in a given figure. A set of three figures, corresponding to MACHI, ALPHAI, and BETAI comprises a complete comparison case. Indicated on each figure is the free-jet test simulated free-stream conditions of flight Mach number (MACH), angle-of-attack (ALPHA), angle-of-sideslip (BETA), and corrected engine face mass flow rate (WC2).

6.1 SUBSONIC COMPARISONS

Two subsonic cases were computed, both for MACH 0.9 and ALPHA 30.0 deg using FBS1. FBS1 has sharp edges and was designed for use at only low BETA values. Case 1 was for BETA 0 deg and represented a high angle-of-attack case where the forebody simulator was not shielding the inlet from the oncoming flow. The combined free-jet nozzle and forebody simulator sidewash angle was − 4.85 deg, and combined angle-of-attack was 33.3 deg. Case 2 was for BETA − 10.0 deg in which the inlet was slightly shielded as a result of the forebody simulator sidewash angle of 7.8 deg and angle-of-attack of 29.2 deg. An insufficient amount of experimental data was in the probe calibration range for Case 2 to justify performing computation-to-experiment comparisons at higher BETA values (at these MACH and ALPHA conditions).

Case 1 comparisons are shown in Fig. 14. MACHI predicted values are within the limits of the experimental data bands over the entire IRP. The computational data indicate that the incoming flow experienced a rapid deceleration immediately upstream of the start of the experimental data, followed by a gradual acceleration as the flow travels aft toward the inlet

throat region. Predicted and experimental ALPHAI values differ significantly, with the largest difference occurring at the most forward IRP locations. The ALPHAI values are larger than experimental values, on the order of 10 to 15 deg. These ALPHAI values suggest that a portion of the IRP flow field is not being aligned with and ingested into the inlet. The predicted BETAI values are within the limits of the experimental data bands for the aft half of the inboard probe locations and over the entire range of the center probe location.

Case 2 comparisons are shown in Fig. 15. MACHI predicted values are in very good agreement with the experimental data bands, with MACHI values being approximately one-half of simulated free-stream 0.9 Mach number. Trends are also correct with the lowest MACHI values at forward IRP locations and higher MACHI values closer to the inlet throat area of the IRP. ALPHAI values are in good agreement over most of the IRP, with the largest difference occurring near the leading edge region of the inlet. The experimental ALPHAI values indicate that the incoming flow is nearly aligned with the inlet ramps over most of the IRP, whereas the computational ALPHAI value plots indicate that flow alignment results from a gradual turning of the incoming flow over the forward half of the IRP. Predicted BETAI values are within the limits of the experimental data bands over all the IRP except at the forward portion of the inboard probe location. A possible source for the prediction error near the inlet leading edge is a large flow separation region appearing in the computations on the top side of the inlet near the leading edge. Should this separation not be realistic, it may significantly alter the slope of streamlines approaching the inlet leading edge region.

The comparisons of the predicted and experimental IRP values indicate that the computations are modeling the mean flow features of the IRP and are consistent with the experimental data trends and uncertainties. The only area of large differences is in the rate and degree to which the IRP flow field turns and aligns with the inlet's internal ramps. Should the inlet leading edge region appear of significant importance, then a more thorough modeling would have to provide greater resolution to the inlet top side flow features for which there is little supporting experimental data. Once again it appears necessary to mention that the computations do not account for some test hardware, such as the inlet cowl actuator.

A summary of the differences between the experimental and computational results is given in the first two columns of Table 4. Included in the summary of each case is the minimum and maximum disagreement as well as the number of comparison points and the average disagreement.

6.2 SUPERSONIC COMPARISONS

Three supersonic 2.2 MACH computations were performed, two at high ALPHA and one at low ALPHA with FBS3. Only the free-jet nozzle was used to create the required ALPHA

16

and BETA conditions during supersonic testing. The basic flow structure consisted of supersonic flow encountering the slightly rounded leading edge of the forebody simulator, thus setting up a bow shock. The flow then accelerated down the side of the forebody simulator until it was again nearly at free-stream Mach number before encountering the inlet. The bow shocks, although considered in the design of the forebody simulators, may have reflected off of the free-jet nozzle walls and back into the IRP (Fig. 16). The supersonic flow entering the inlet created a set of shocks originating at the cowl leading edge and three ramp junctures. The final shock forced the flow to be subsonic upstream of the inlet throat.

Case 3 (Fig. 17) corresponds to an ALPHA of 12 deg and BETA of 3 deg which required a free-jet nozzle angle-of-attack of 8.7 deg and sidewash angle of 6.5 deg. The difference between predicted values and experimental data bands for MACHI is up to 0.48 upstream of where the inlet shock structure is believed to cross the IRP. Locations where the inlet shock structure cross the IRP are very sensitive to the local, probably subsonic, flow field at the inlet's lower lip. CFD planar contour plots indicate that the reflected forebody simulator bow shock may also pass through the IRP at nearly the same location. The predicted ALPHAI values indicate the presence of a wave passing through the IRP just upstream of where the inlet shock structure crosses the IRP. This wave may be the reflected bow shock since it slightly increases the ALPHAI values, as would an upward and rearward running shock wave. The predicted and experimental ALPHA values are nearly the same over the entire inboard probe location. The predicted ALPHAI are a nearly constant 2 to 3 deg lower than the experimental values at the center probe location. Both the experimental and computational BETAI values show the presence of possibly several waves, including one strong shock wave near the aft portion of the IRP. The differences in values vary from 0 to 5 deg, with the smallest differences occurring at the inboard IRP location.

Case 4 (Fig. 18) corresponds to 12 deg ALPHA and 0 deg BETA, which required free-jet nozzle settings of 9.13 deg in angle-of-attack and 1.7 deg in sidewash angle. Both the experimental and predicted values of MACHI indicate the presence of at least two waves passing through the IRP. One wave is located where the inlet ramp shock structure should cross the IRP, which is near the aft of the IRP. The second presumed wave is more forward near an IRP value of 9.6 in. The origin of this wave is not understood, but appears to affect the experimental BETAI values slightly and the ALPHAI values not at all, indicating a sideways running wave. The difference in predicted and experimental values is as great as 0.13 in MACHI. The experimental and predicted ALPHAI values indicate the presence of a wave at IRP value of 3.2, which is presumed to be the reflected forebody simulator bow shock, as it was presumed to be in Case 3. The predicted ALPHAI values are less than the experimental values by 1.5 to 2.5 deg for the center probe location and within the limits of the experimental data band for most of the inboard probe location. Both the experimental and predicted BETAI values respond to the 3-deg decrease in BETA from Case 3 (Fig. 17c) in the middle of the

IRP. The response is least for the inboard probe and greatest for the center probe. The predicted BETAI values are generally within the limits of the experimental data band for the inboard probe and less than experimental values for the center probe with a maximum experimental-to-predicted difference of 4 deg.

Case 5 (Fig. 19) corresponds to an ALPHA of 0 deg and BETA of 0 deg, which required a free-jet nozzle angle-of-attack of −4.8 deg and sidewash angle of 3.7 deg. As in Case 4, both the experimental and predicted values of MACHI indicate multiple waves passing through the IRP. This is shown in Fig. 16b as well as in Fig. 19a by the local minimums and maximums in Mach number as the length of the IRP is traversed. The difference in predicted and experimental MACHI values is as great as 0.24. The experimental ALPHAI values indicate the presence of two waves, one at an IRP value of 3.0 in. and another at a value of 6.0 in. The predicted ALPHAI values are greater than experimental values by up to 7 deg for the inboard probe location and within the limits of the experimental data band for the center probe location. The experimental BETAI values agree well with the predicted values except for low IRP values on the inboard probe with a maximum deviation of 9 deg.

The maximum Mach number at which the probes were calibrated was 2.0 (limitation imposed by calibration of Tunnel 4T operational range). Since the supersonic experimental data presented generally exceeded a Mach number of 2.0, the uncertainty in the presented comparisons was increased. The assumption made prior to calibrating the probes is that a Mach 2.0 calibration is also sufficient for determining local Mach numbers above Mach 2.0. As for the subsonic cases, a summary of the disagreement between experimental and computational data is given in the third, fourth, and fifth columns of Table 4.

7.0 OBSERVATIONS AND CONCLUSIONS

Observations and conclusions resulting from this effort are restated as follows:

1. The F-15 free-jet inlet model was an appropriate geometry to determine the IRP prediction accuracy of the PARC3D code being representative of fighter-like configurations.

2. Detailed experimental information required to perform the computations was readily available and believed accurate.

3. The model complexity downstream of the inlet, in the region of support test hardware, was approximated in the subsonic computational model.

4. A portion of the experimental data had to be considered unsuitable and was not used for CFD code comparison because measured total flow angles exceeded the probe calibration range.

5. The main contributor to the experimental uncertainty magnitude was the probe calibration curve fit used for cases where combined flow angles were larger than the normal operating range of the probe, but still were within calibration range.

6. Supersonic experimental data at a Mach number of 2.2, which were compared to predicted CFD values, generally exceeded the maximum probe calibration Mach number of 2.0. The assumption was made that the Mach 2.0 calibration could be extrapolated to Mach numbers above 2.0, which introduced an undetermined amount of experimental uncertainty.

7. Based on the comparisons presented herein, an estimate of prediction accuracy has been determined relative to 1/6-scale F-15 free-jet inlet model experimental data (Table 4). The quoted accuracy is a strong function of both CFD introduced approximations and experimental uncertainty. The prediction accuracy is stated separately for each computational case by indicating the range of differences between predicted IRP values and truth. Therefore, the predicted value may be either greater than or less than truth by as much as the prediction accuracy amount stated in Table 4. In addition, the overall average differences between the actual and predicted IRP parameters are given in the last column of Table 4.

8. The experimental uncertainty is generally of the same order-of-magnitude as the maximum prediction error stated in Item 7.

The objective of the CFD effort was achieved in that a measure of the code's ability to predict specific inlet flow parameters was obtained; however, facts presented in Items 3 through 6 and 8 may have decreased the utility of the information presented in Item 7. The information presented in Item 7 would have certainly been more valuable if (1) the free-jet model had been more aerodynamically clean and, therefore, more accurately modeled computationally; (2) the experimental uncertainty magnitudes had been smaller so that a more accurate determination of the difference between the predicted values and truth could have been determined; and (3) the probe calibration range had covered the full range of the measured experimental data so that valuable experimental data did not have to be deemed unusable for this effort.

The overall results of this effort are encouraging. A complex geometry and test procedure were simulated with a general purpose production CFD code, PARC3D. The IRP comparison

data demonstrated that many of the gross features of the flow-field such as compression and expansion waves as well as shocks were correctly predicted. Their effects at the IRP were evident by close examination of the plotted data. For example, both the experimental and computational results for Case 5 Mach number, center probe position, showed a compression wave at 5.0 in. on the IRP and an expansion wave at 8.2 in. Future plans include adding viscous wall boundary conditions as well as improved computational gridding. The goal of these two improvements is better modeling of the physics of the free-jet flow field, resulting in closer agreement between experimental and computational data. One of the most important observations that can be made relative to the overall experimental and computational effort is that by continuing to work these two separate disciplines in close cooperation (in time, location, and personnel), ultimately a superior analysis and evaluation capability will develop.

REFERENCES

1. Mitchell, J. G. "A New Test Capability for Propulsion System Testing." AIAA Paper No. 73-1283, 9th Propulsion Conference, November 5-7, 1973.

2. Beale, D. K. "Evaluation of a Free-Jet Technique for Testing Fighter Aircraft Propulsion Systems." AIAA Paper No. 86-1460, AIAA/ASME/SAE/ASEE 22nd Joint Propulsion Conference, June 16-18, 1986.

3. Huddleston, D. H. and Mastin, C. W. "Optimization of Aerodynamic Designs Using Computational Fluid Dynamics." AGARD Specialists Meeting on Computational Methods for Aerodynamic Design (Inverse) and Optimization, Loen, Norway, May 1989.

4. Beale, D. K. and Collier, M. S. "Validation of a Free-Jet Technique for Evaluating Inlet-Engine Compatibility." AIAA Paper No. 89-2325, AIAA/ASME/SAE/ASEE 25th Joint Propulsion Conference, July 10-12, 1989.

5. Abernethy, R. B. and Thompson, J. W. "Handbook, Uncertainty in Gas Turbine Measurements." AEDC-TR-73-5 (AD-755356), February 1973.

6. Cooper, G. K. and Sirbaugh, J. R. "The PARC Distinction: A Practical Flow Simulator." AIAA Paper No. 90-2002, AIAA/ASME/SAE/ASEE 26th Joint Propulsion Conference, Orlando, Florida, July 1990.

7. Beam, R. M. and Warming, R. F. "An Implicit Scheme for the Compressible Navier Stokes Equations." AIAA Paper No. 77-645, AIAA 3rd Computational Fluid Dynamics Conference, June 1977.

8. Pulliam, T. H. and Steger, J. L. "On Implicit Finite-Difference Simulations of Three-Dimensional Flow." AIAA Paper No. 78-10, AIAA 16th Aerospace Science Meeting, January 1978.

9. Jameson, A., Schmidt, W., and Turkel, E. "Numerical Solutions of the Euler Equations by Finite Volume Methods Using Runge-Kutta Time-Stepping Schemes." AIAA Paper No. 81-1259, AIAA 14th Fluid and Plasma Dynamics Conference, Palo Alto, California, 1981.

10. Dietz, W. E. and Suhs, N. E. "PEGSUS 3.0: User's Manual." AEDC-TR-89-7 (AD-A211974), August 1989.

FBS1
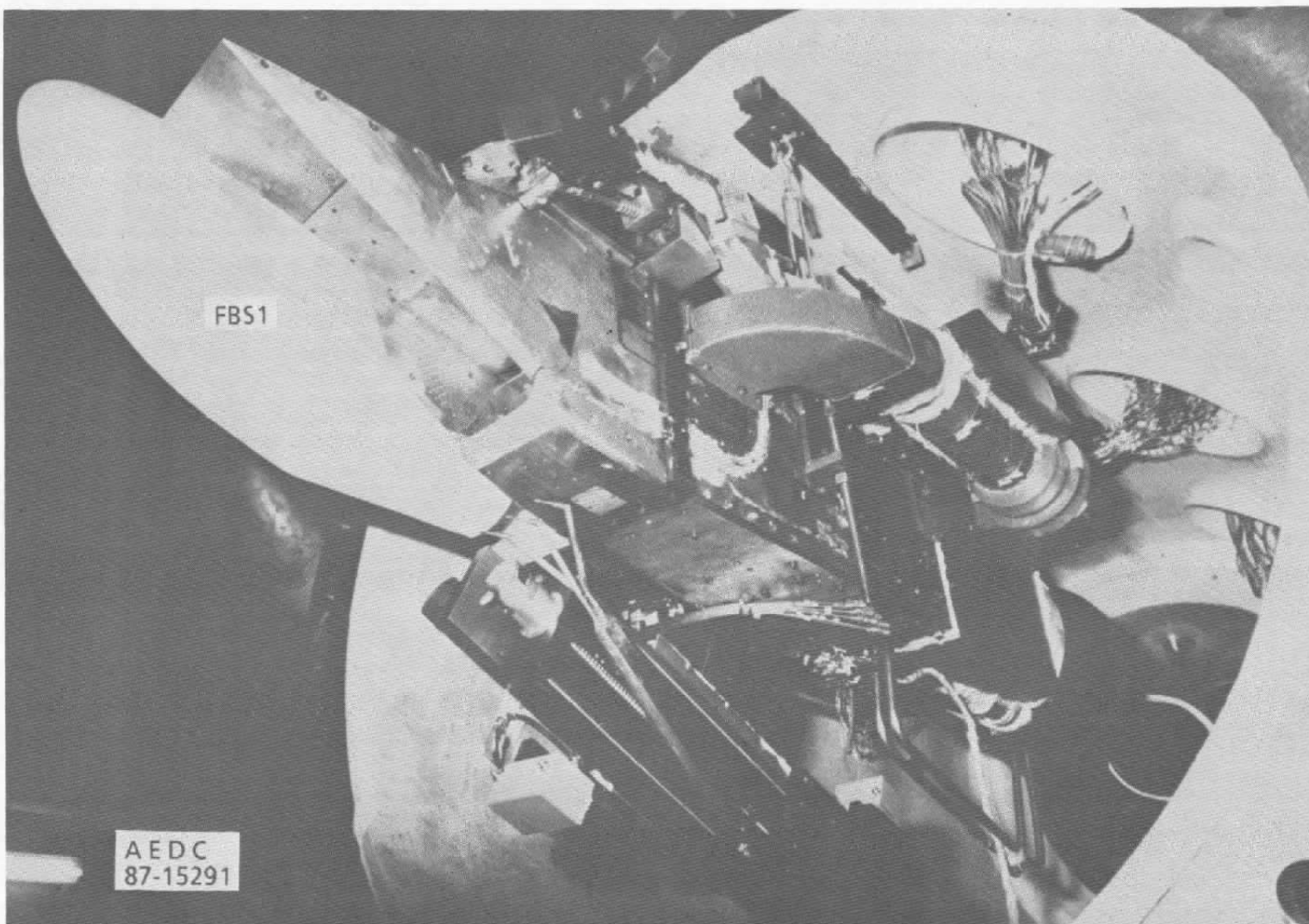
AEDC
87-15291

a. Test cell installation
Figure 1. 1/6-Scale F-15 model in the AEDC pilot free-jet test facility (R2A2).
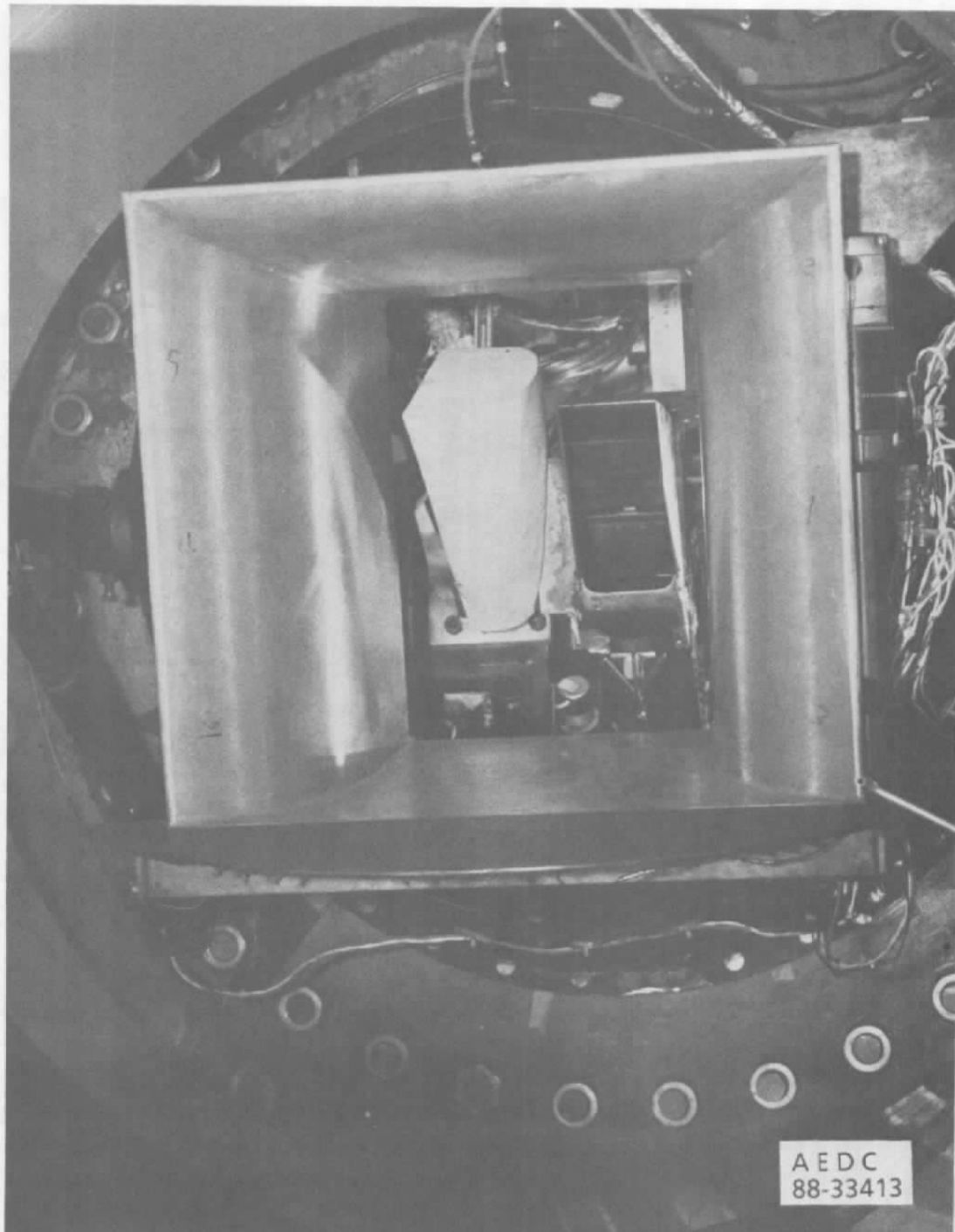
b. View of subsonic test cell with FBS4
Figure 1. Concluded.

Fuselage Top Centerline

Inlet Ramps

IRP

3.1 in.

Rake Position

M_∞

Fuselage Bottom
Centerline
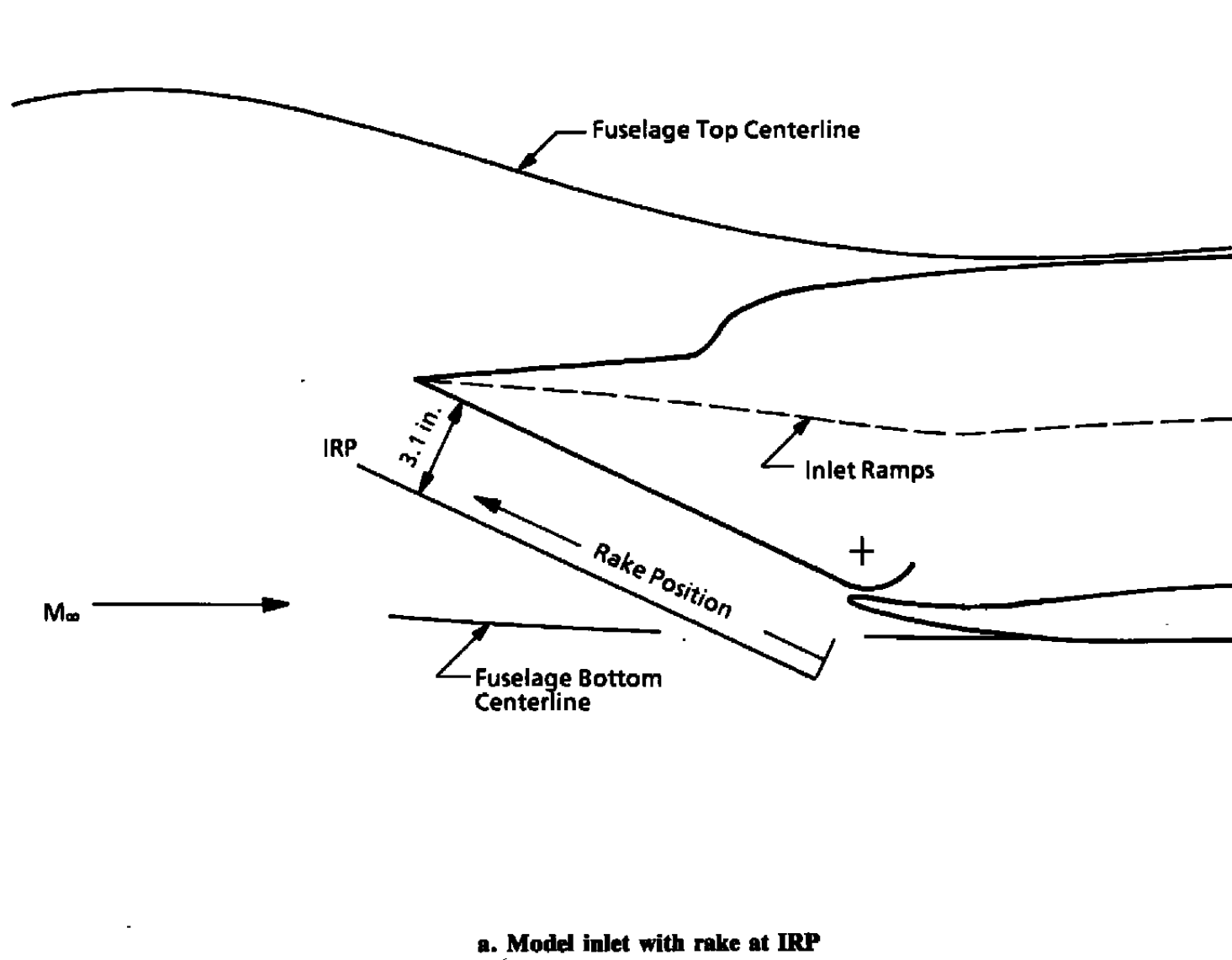
a. Model inlet with rake at IRP
Figure 2. Survey rake and probe geometries.

0.020 Typ.

15 deg

0.125

0.183

0.233

All Dimensions in Inches
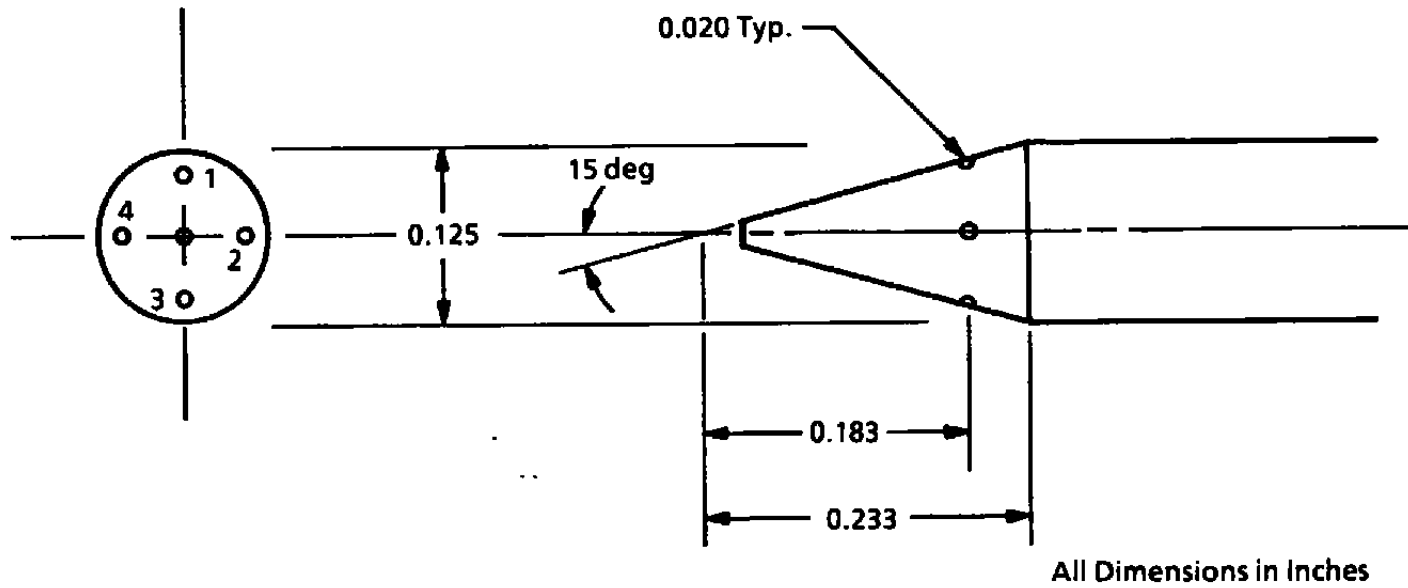
b. Probe tip detail
Figure 2. Continued.

Probe 1

Probe 2

1.45

Probe 3

1.45

Flow

All Dimensions in Inches
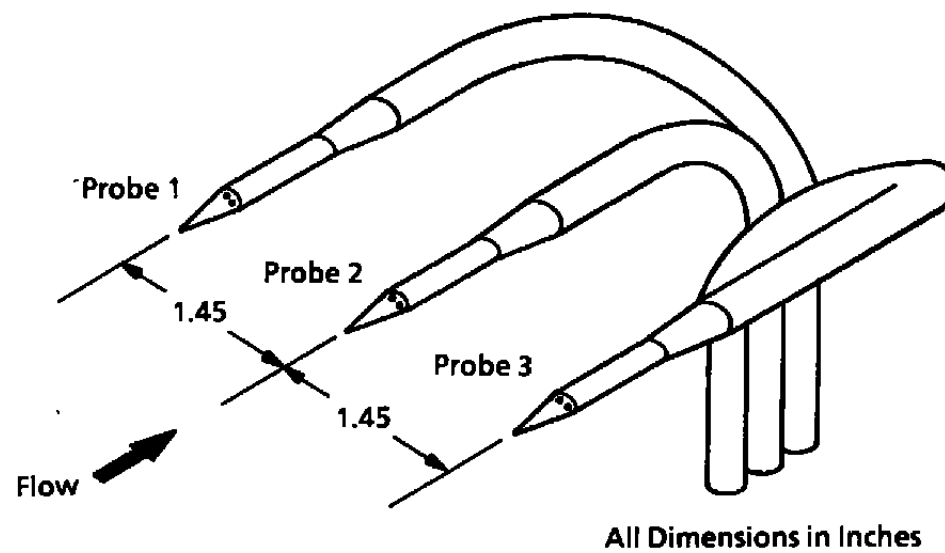
c. IRP rake assembly
Figure 2. Concluded.

$$ALPHAI = ALPHAP + RANGLE$$
$$BETAI = BETAP$$
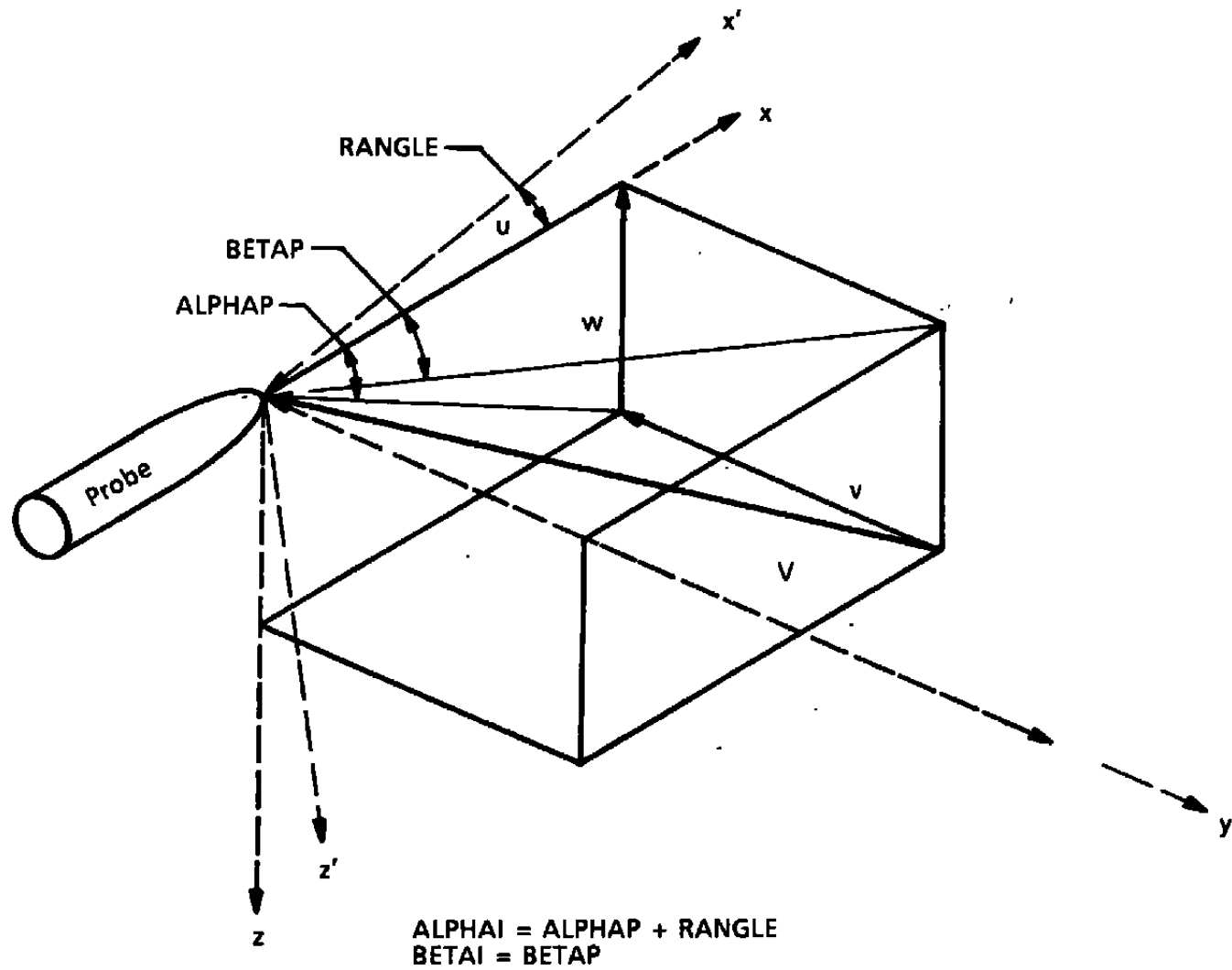
Figure 3. Flow angle definitions.
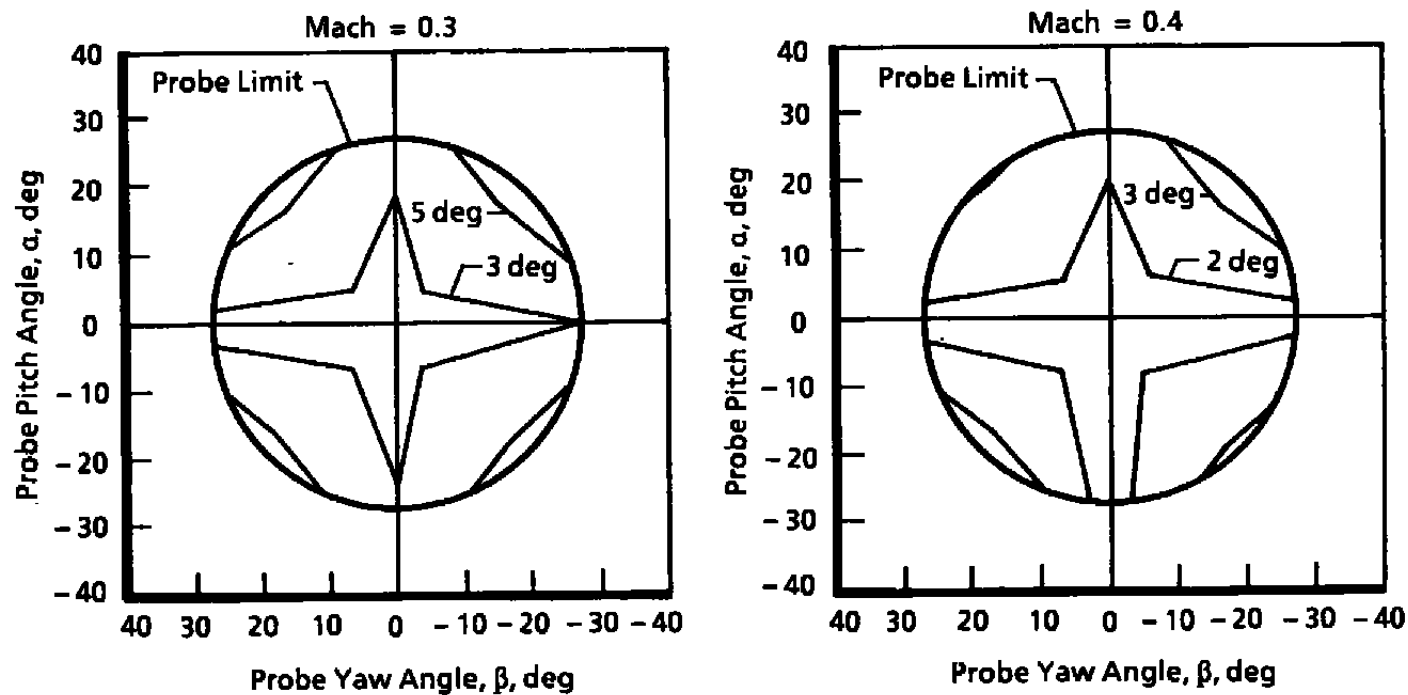
a. Mach = 0.3 and 0.4
Figure 4. ALPHAI uncertainty.
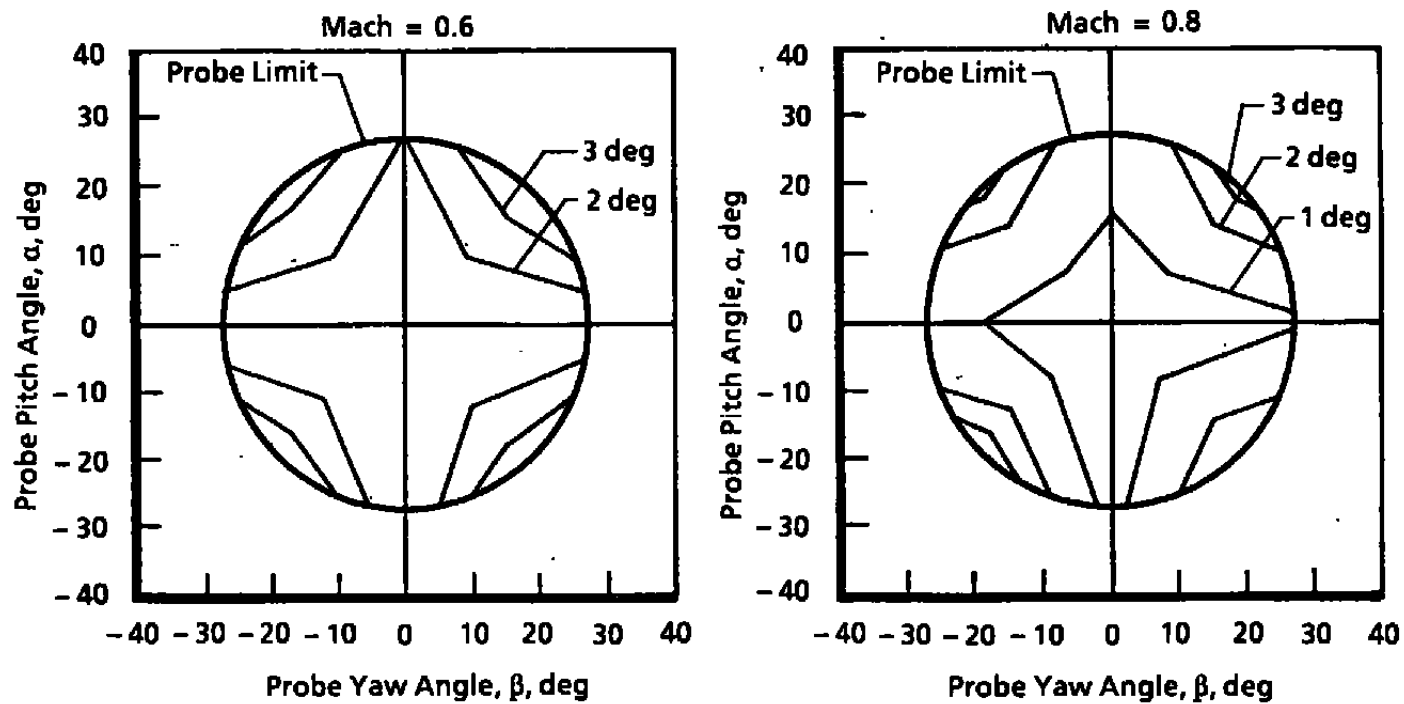
b. Mach = 0.6 and 0.8
Figure 4. Continued.
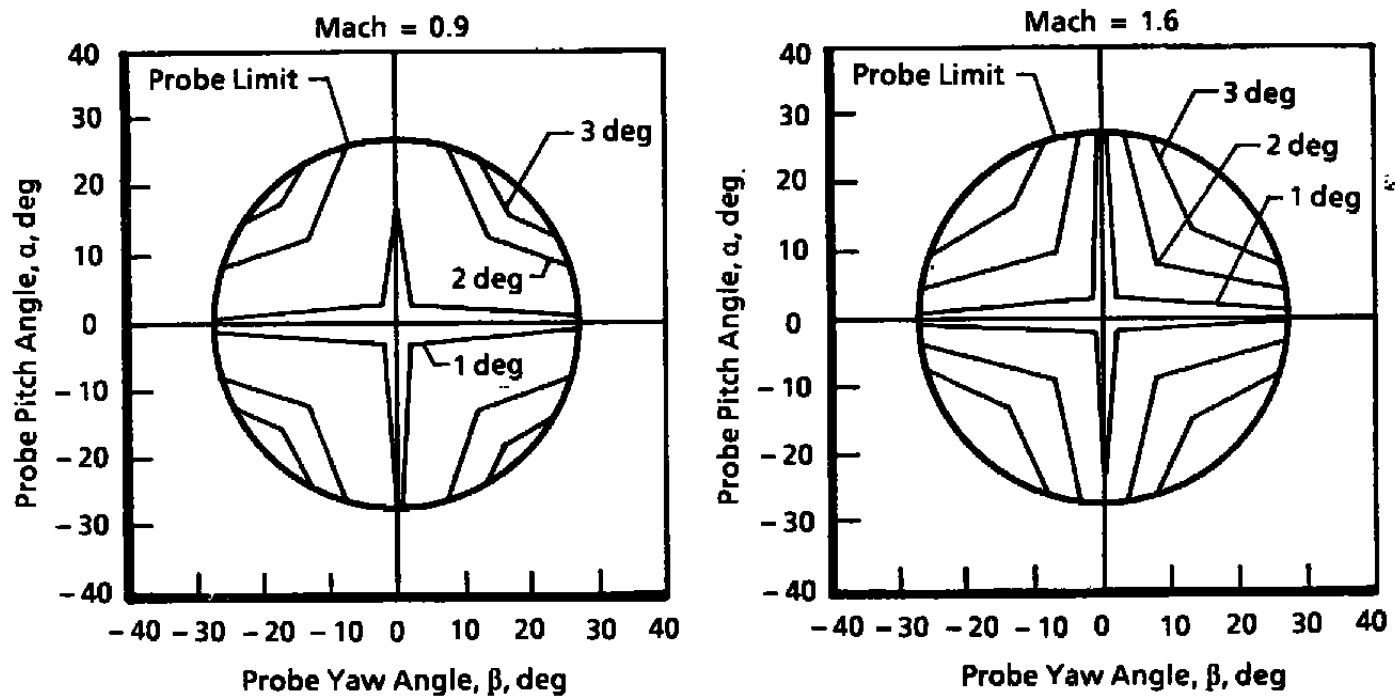
c. Mach = 0.9 and 1.6
Figure 4. Continued.
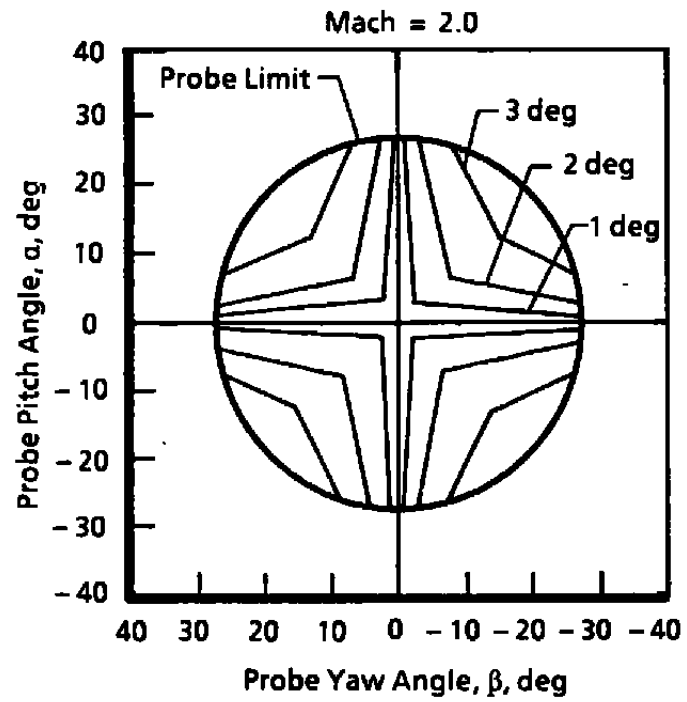
d. Mach = 2.0
Figure 4. Concluded.
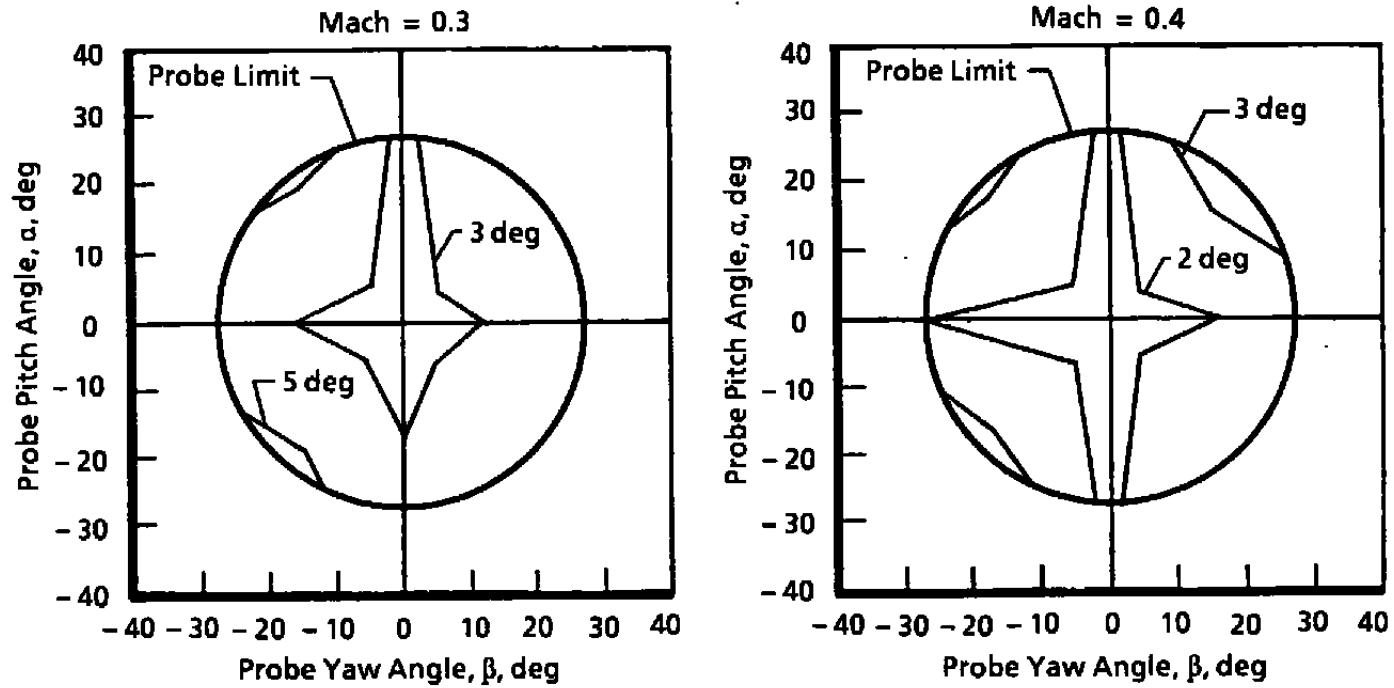
Mach = 0.3

Mach = 0.4

a. Mach = 0.3 and 0.4
Figure 5. BETAI uncertainty.
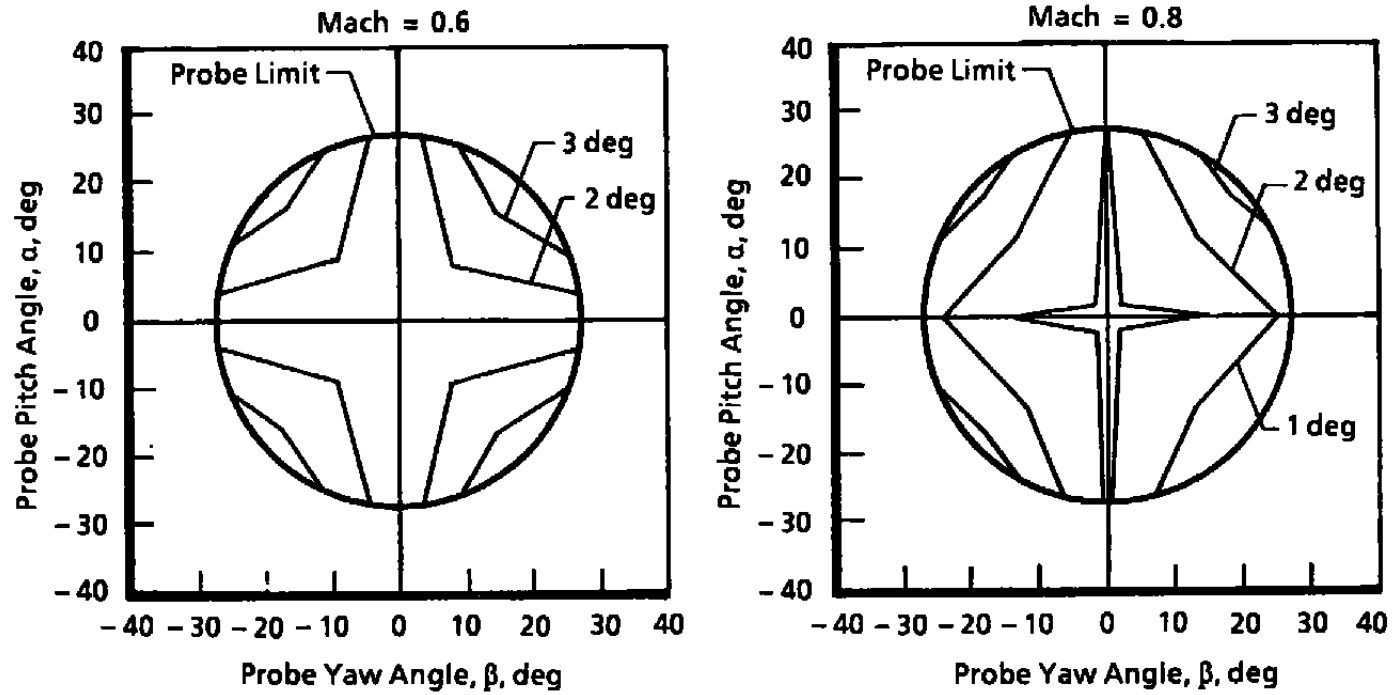
b. Mach = 0.6 and 0.8
Figure 5. Continued.

Mach = 0.9

Mach = 1.6
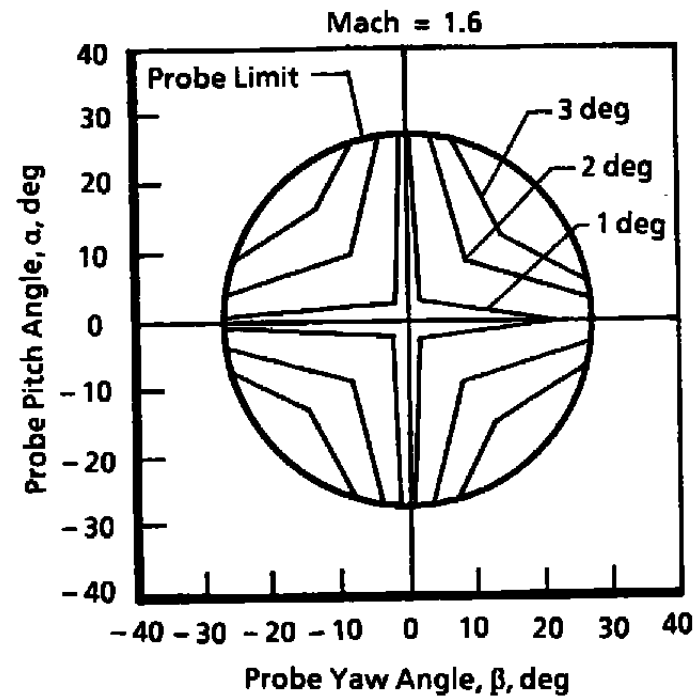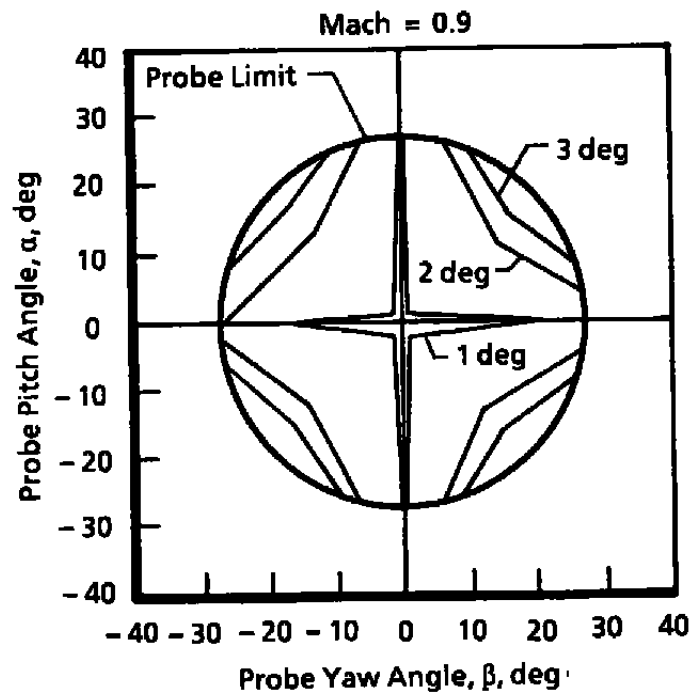
c. Mach = 0.9 and 1.6
Figure 5. Continued.
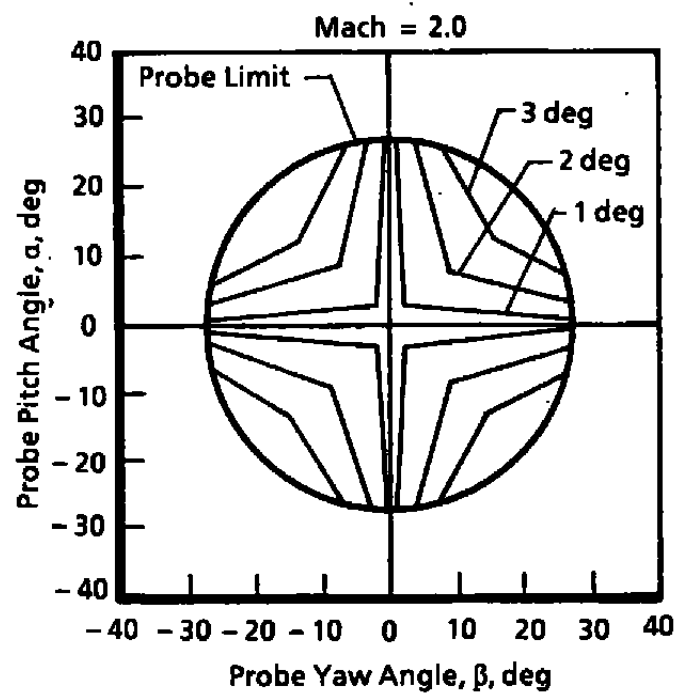
Mach = 2.0

d. Mach = 2.0
Figure 5. Concluded.
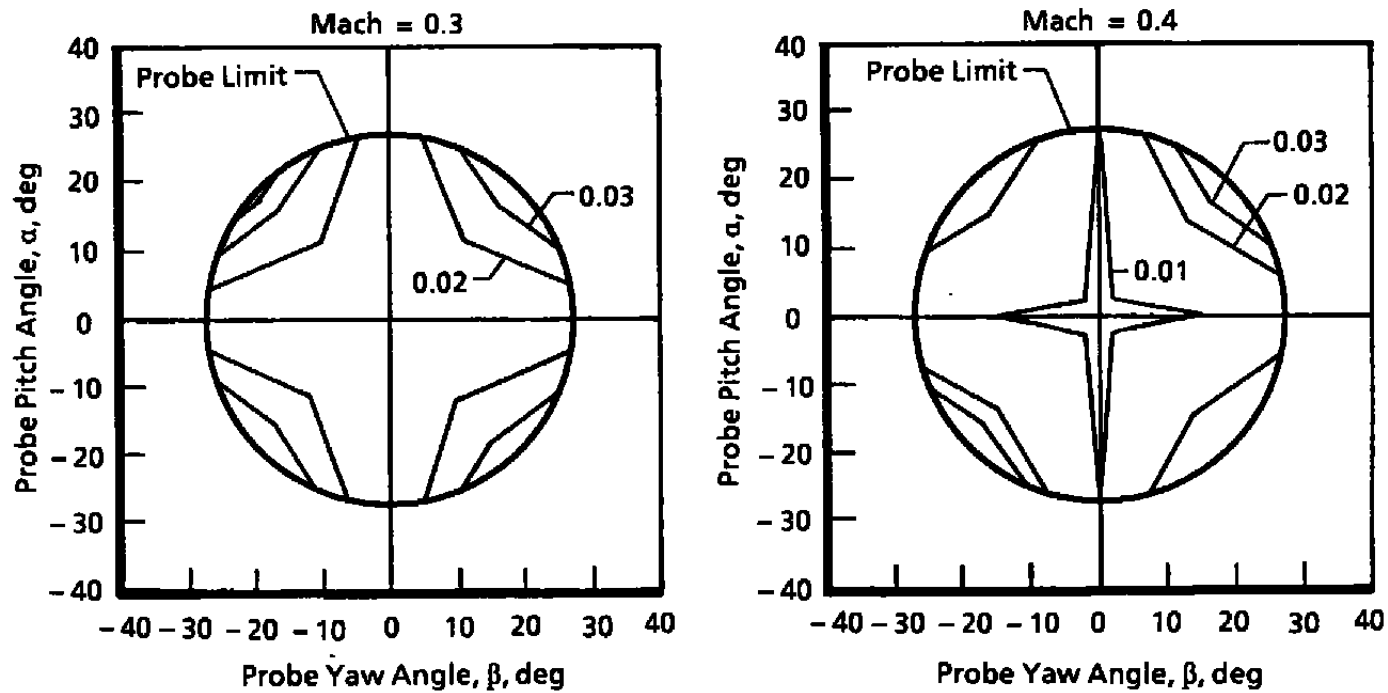
a. Mach = 0.3 and 0.4
Figure 6. MACHI uncertainty.
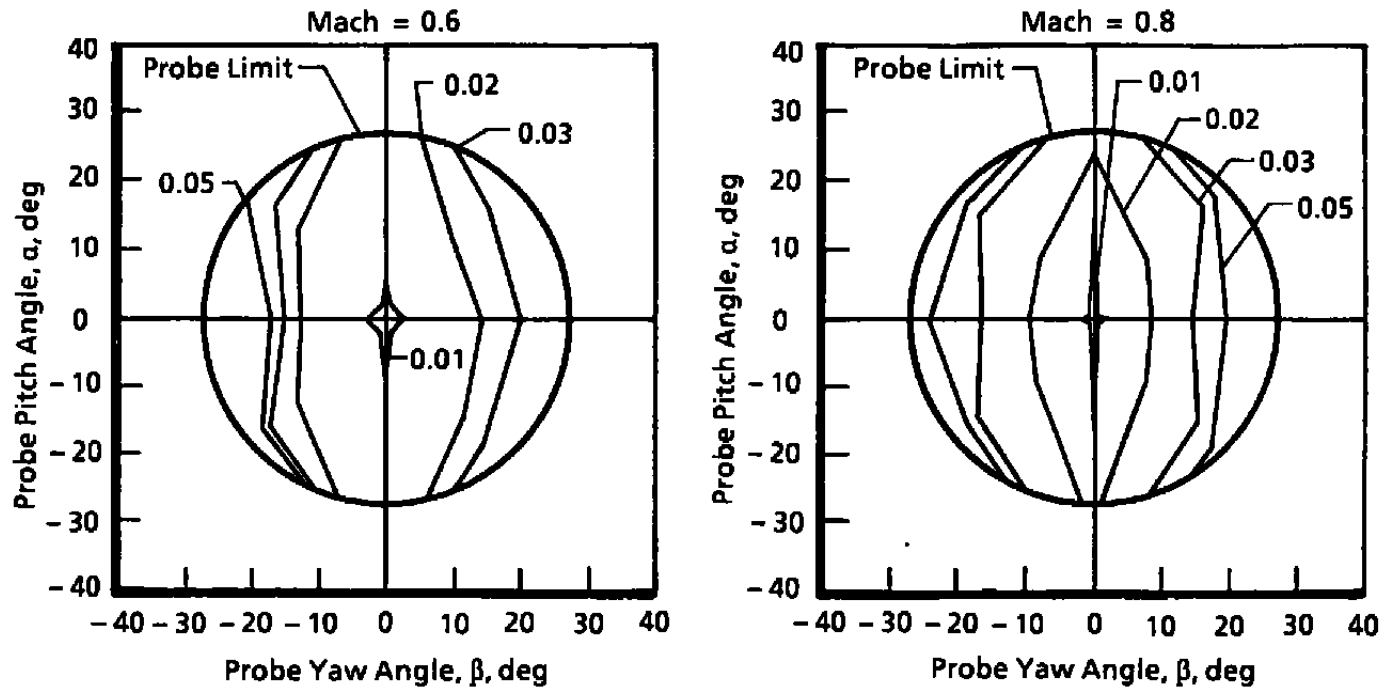
b. Mach = 0.6 and 0.8
Figure 6. Continued.
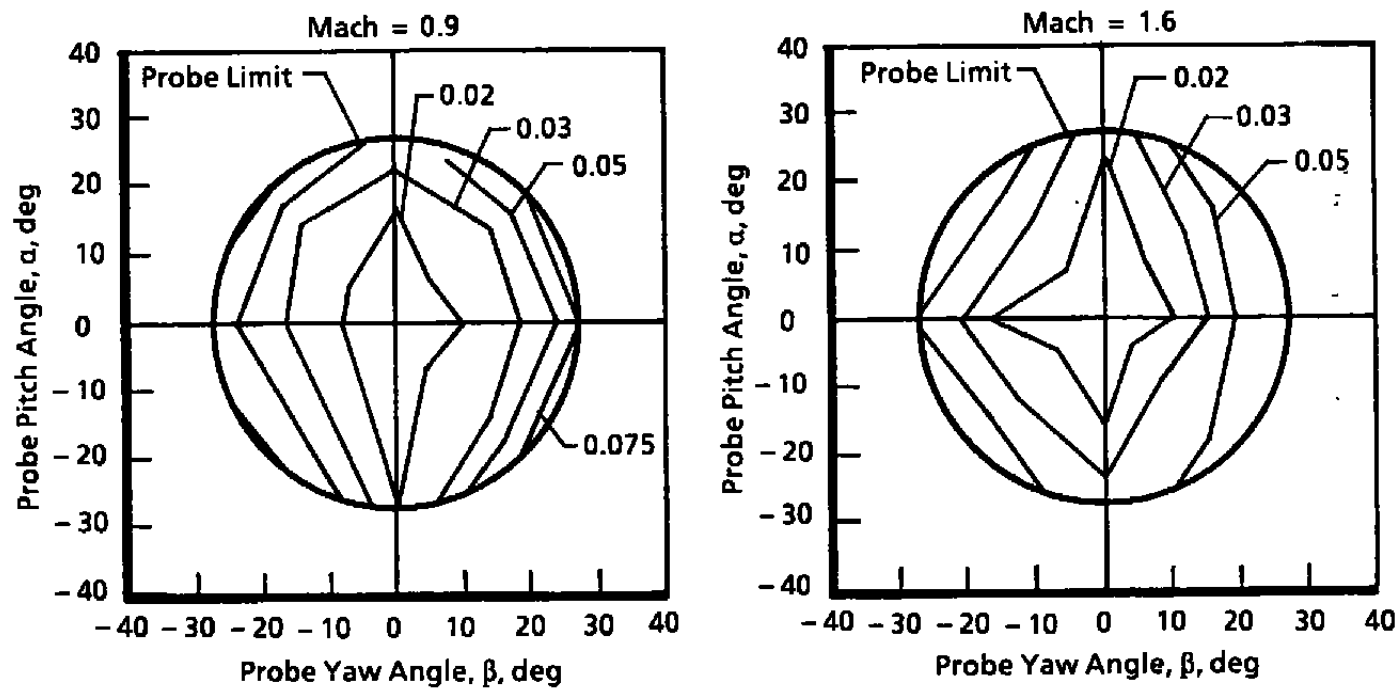
c. Mach = 0.9 and 1.6
Figure 6. Continued.
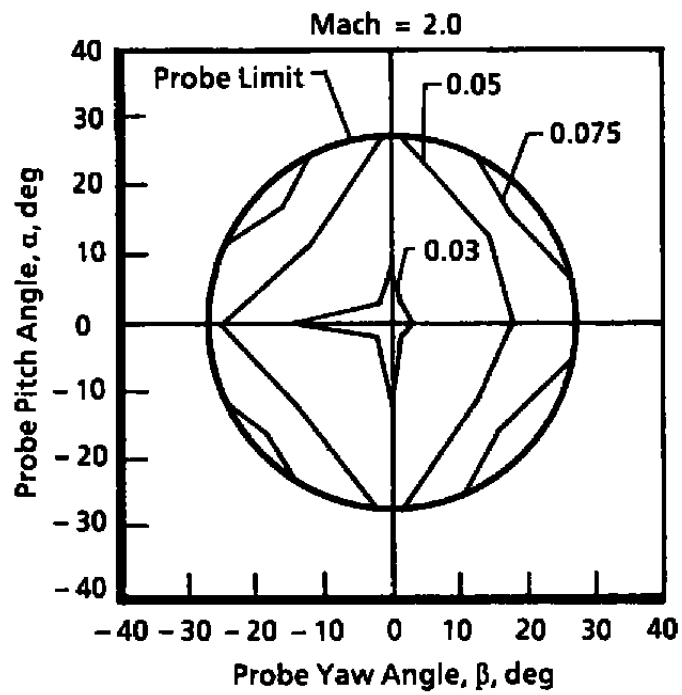
d. Mach = 2.0
Figure 6. Concluded.
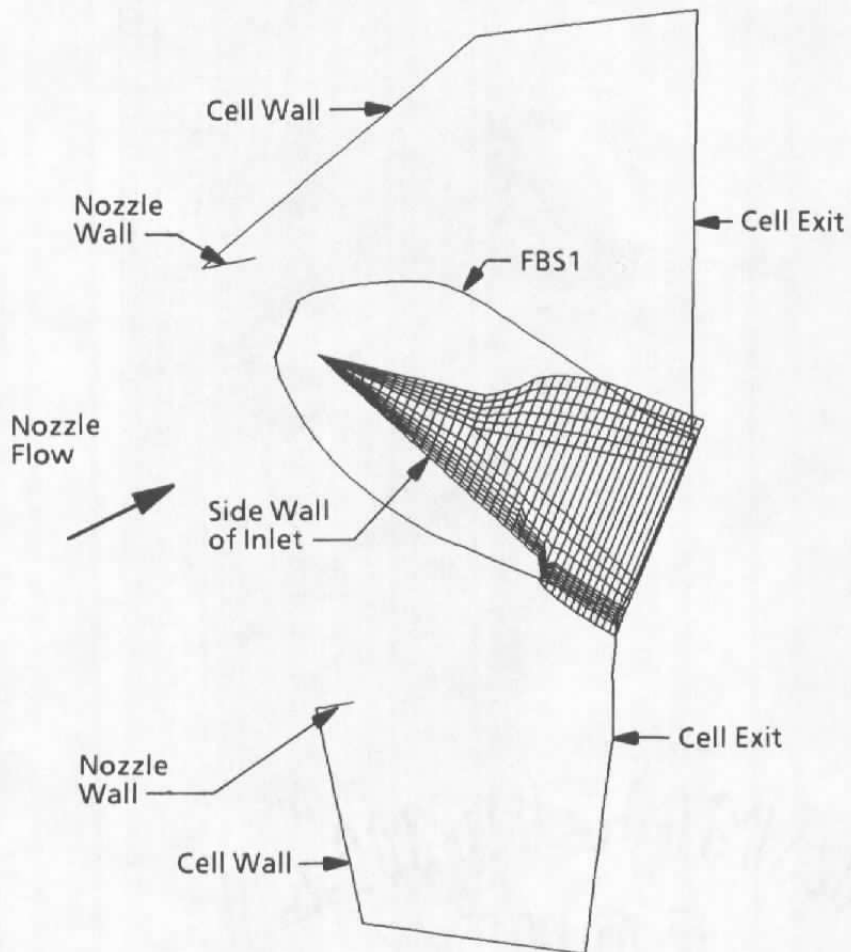
Figure 7. Subsonic grid topology.
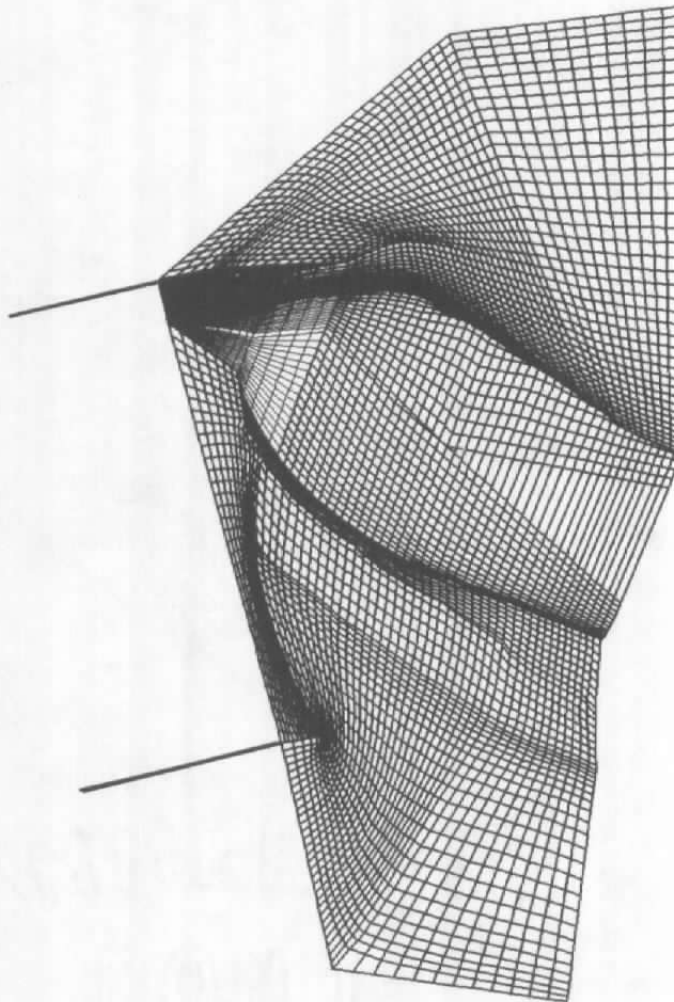
a. Streamwise section of grid including, FBS1 surface grid
Figure 8. Selected subsonic grid plots.
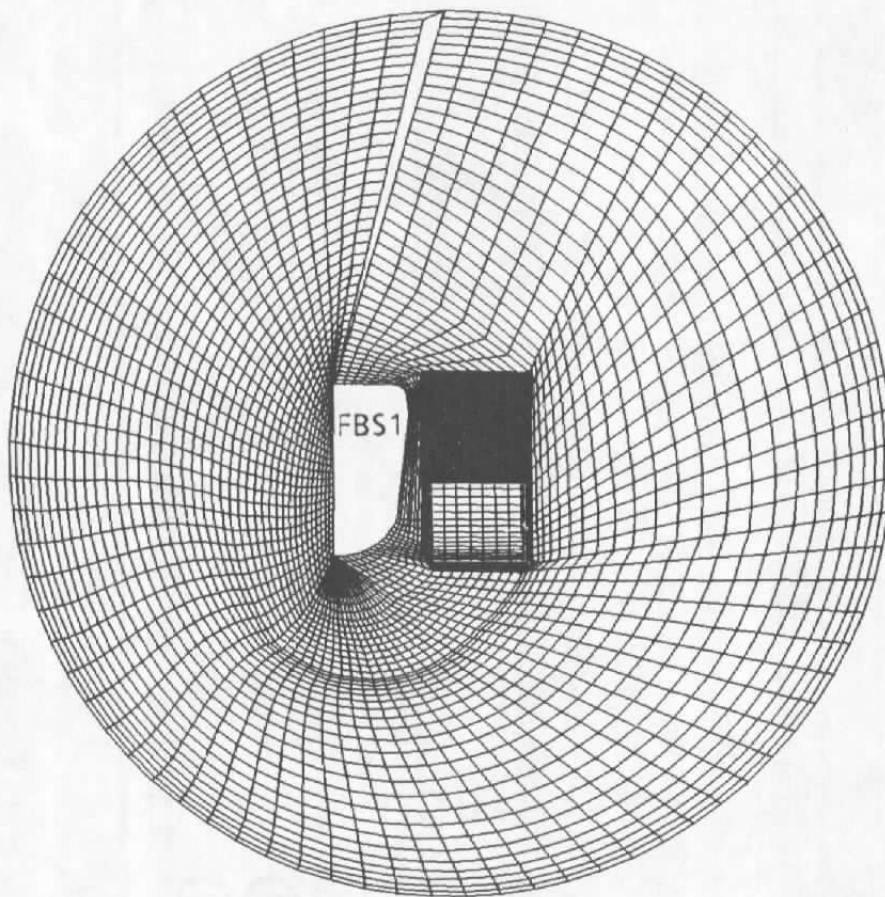
Cell Wall

b. Exit plane grid
Figure 8. Continued.
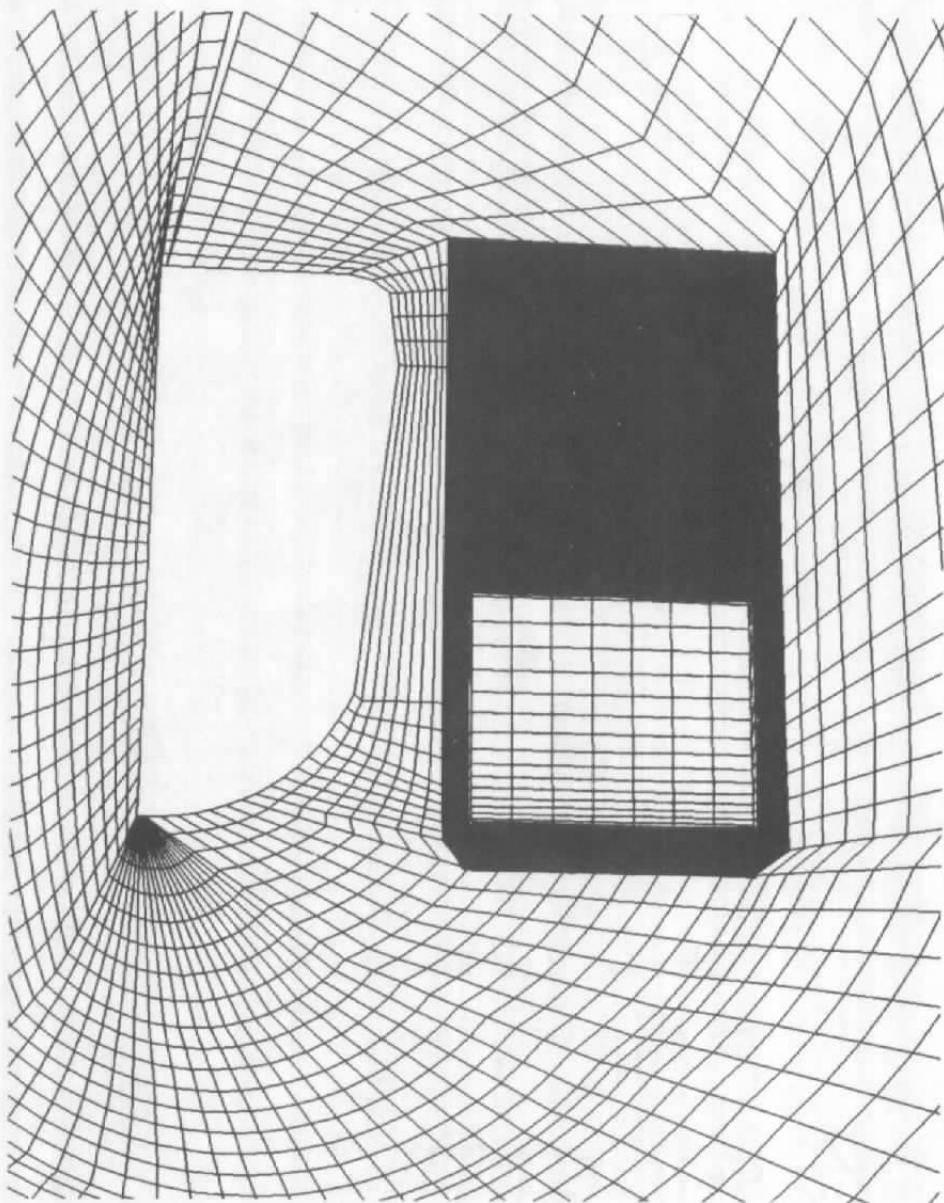
c. Inlet structure in exit plane grid
Figure 8. Continued.
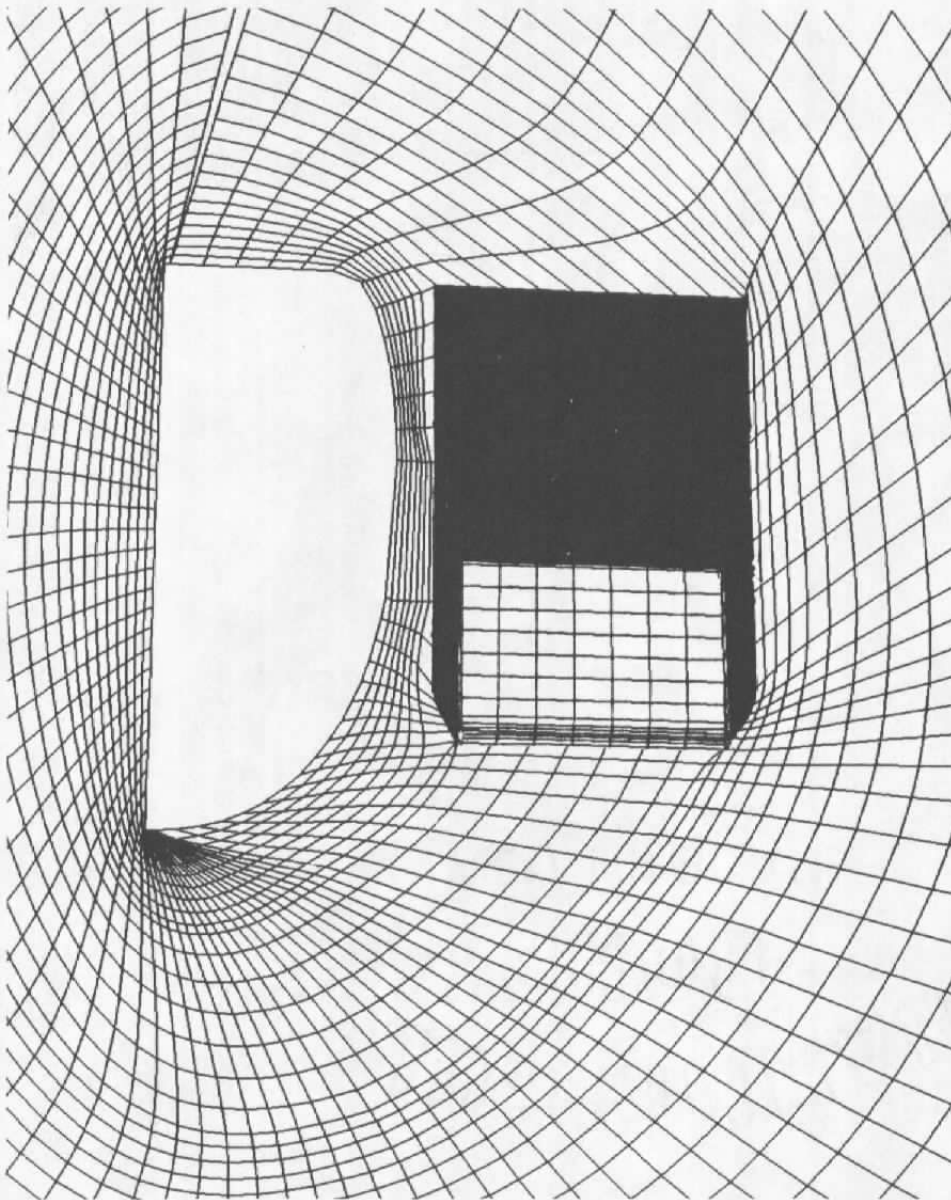
d. Inlet structure of lower lip
Figure 8. Concluded.
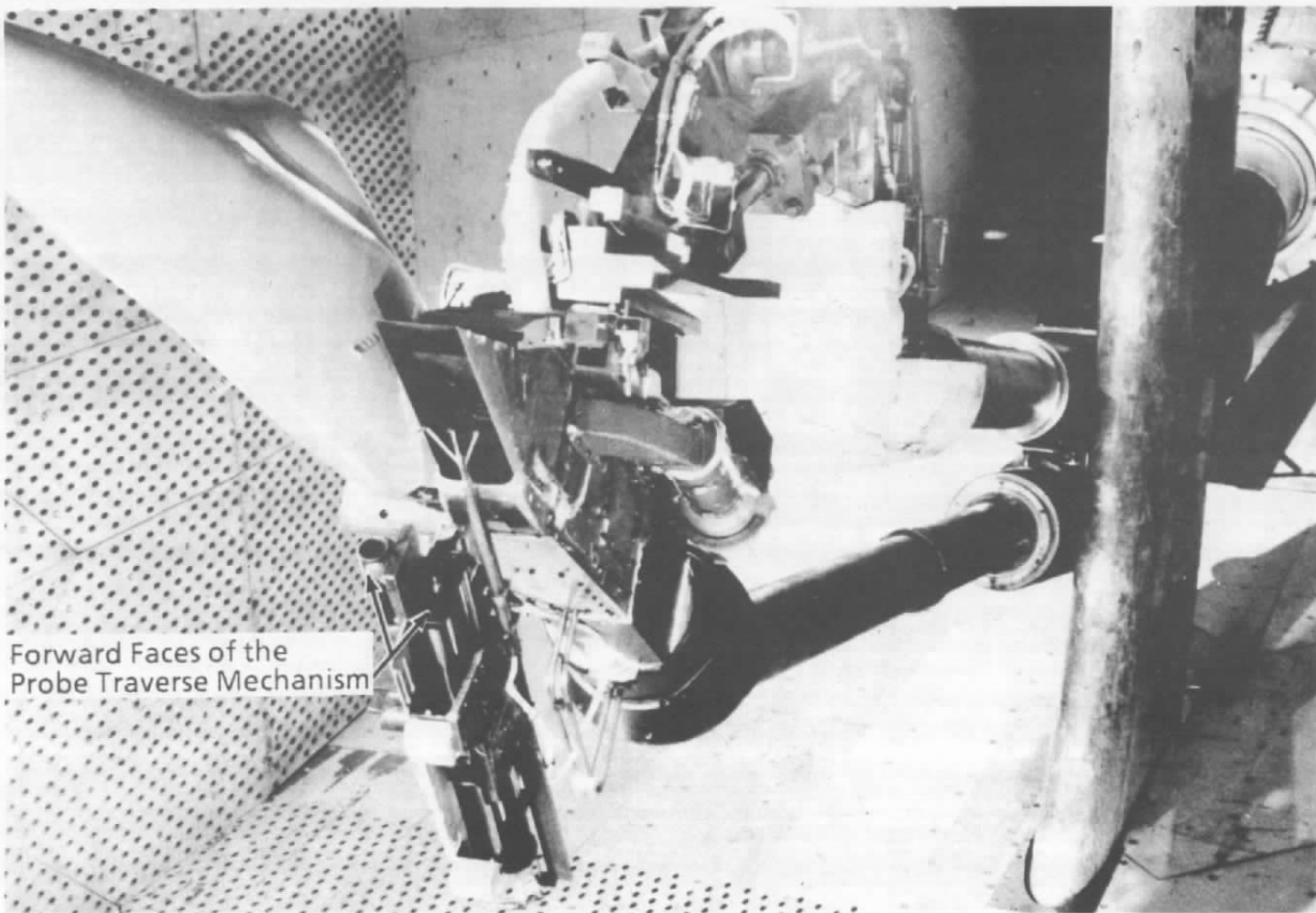
Forward Faces of the
Probe Traverse Mechanism

Figure 9. Probe traverse mechanism.
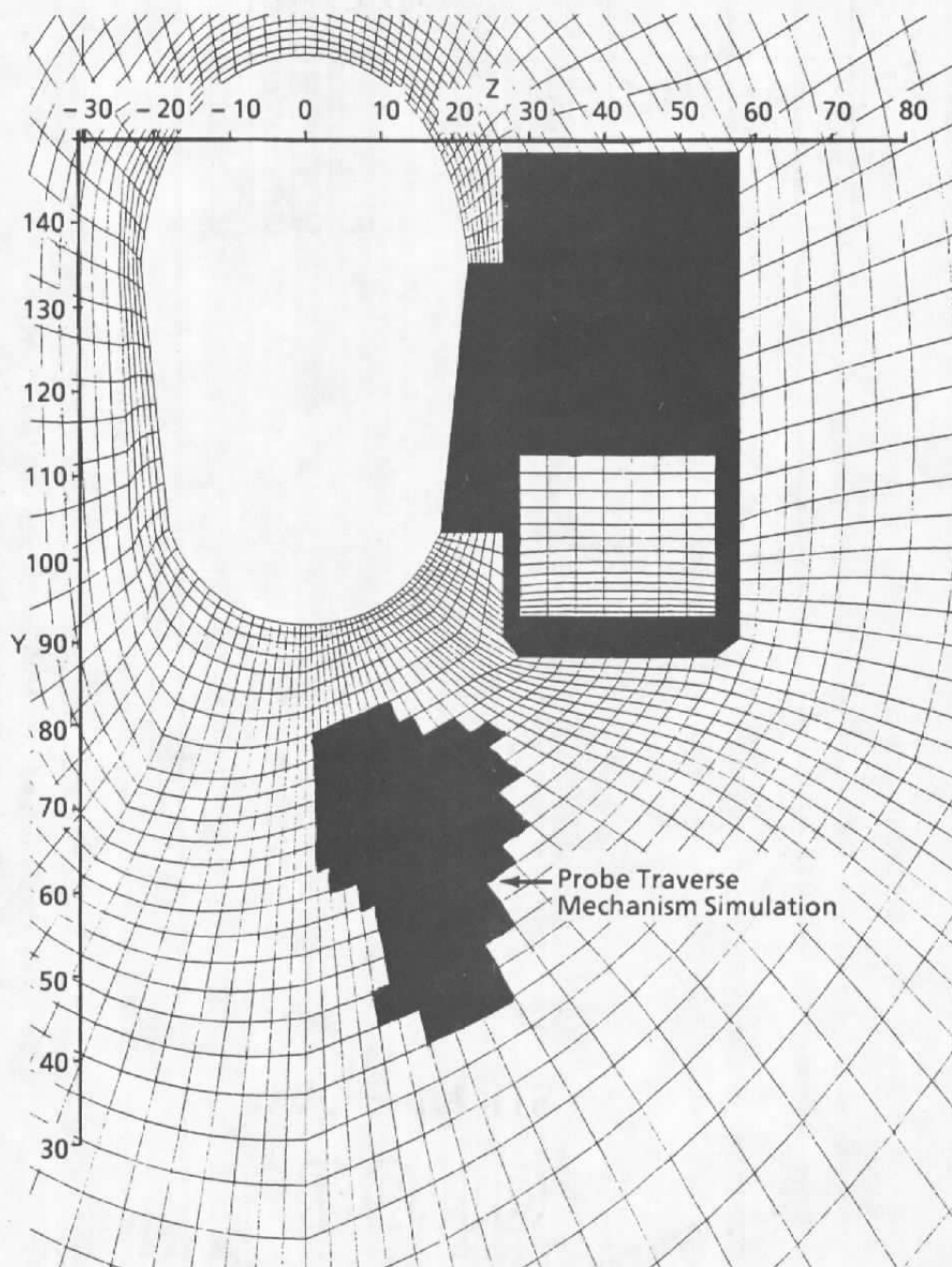
Figure 10. Computational model of probe traverse mechanism.

Cell Grid (Two Blocks)

Inlet

Nozzle Grid (Five Blocks)

Forebody
Simulator

Flow
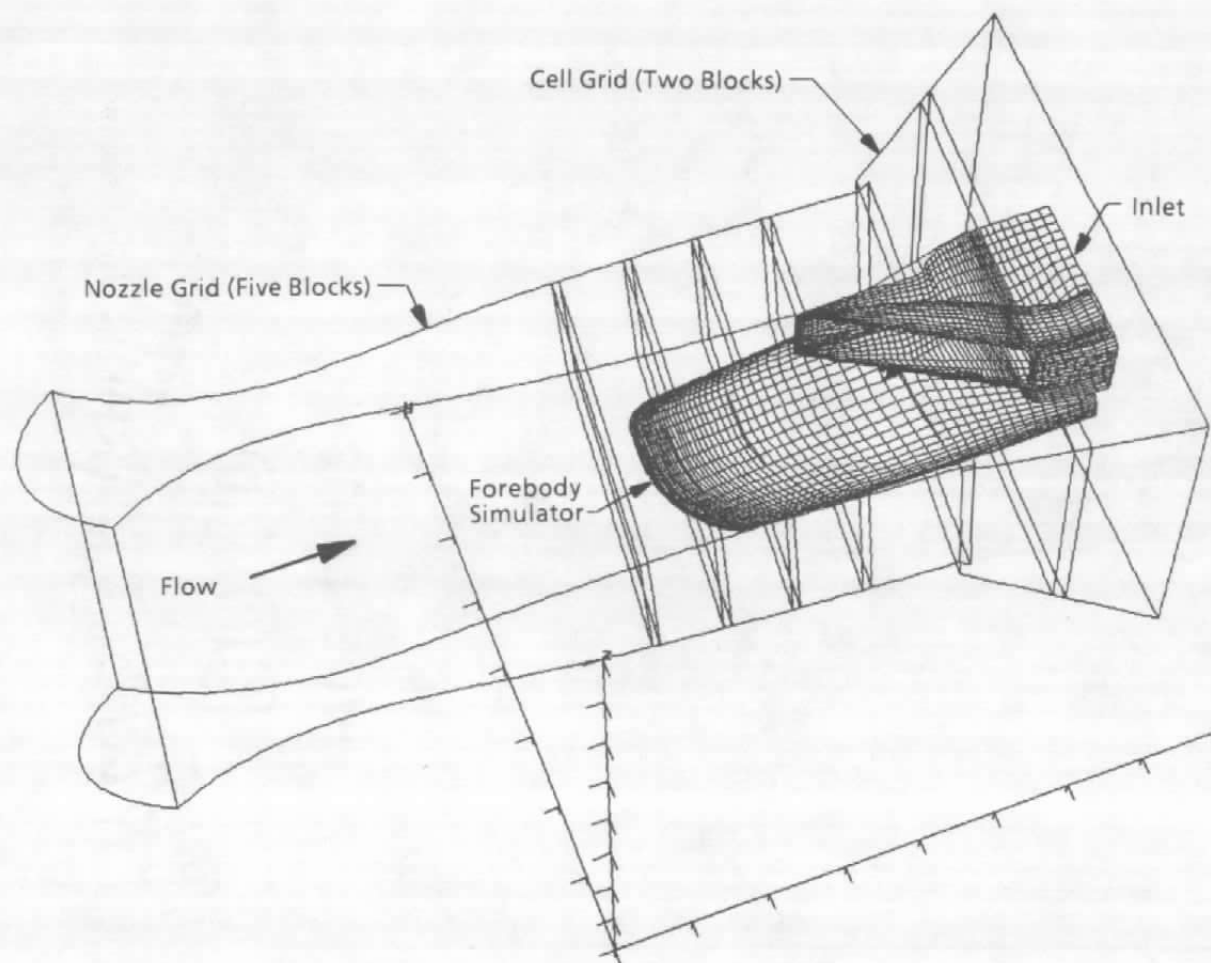
Nozzle: Blocks 1 to 5
Cell: Blocks 6 to 7
Forebody
Simulator: Blocks 8 to 12
Inlet: Blocks 13 to 14

Grid Dimensions	Grid
69 by 5 by 61	1
11 by 61 by 61	2
11 by 61 by 61	3
11 by 61 by 61	4
11 by 61 by 61	5
9 by 69 by 69	6
9 by 69 by 69	7
13 by 59 by 59	8
15 by 59 by 59	9
15 by 59 by 59	10
15 by 59 by 59	11
15 by 59 by 59	12
61 by 41 by 20	13
61 by 41 by 21	14

a. Forebody simulator and inlet with nozzle and cell block overlaps
Figure 11. Supersonic blocking strategy.

Holes Cut in Nozzle
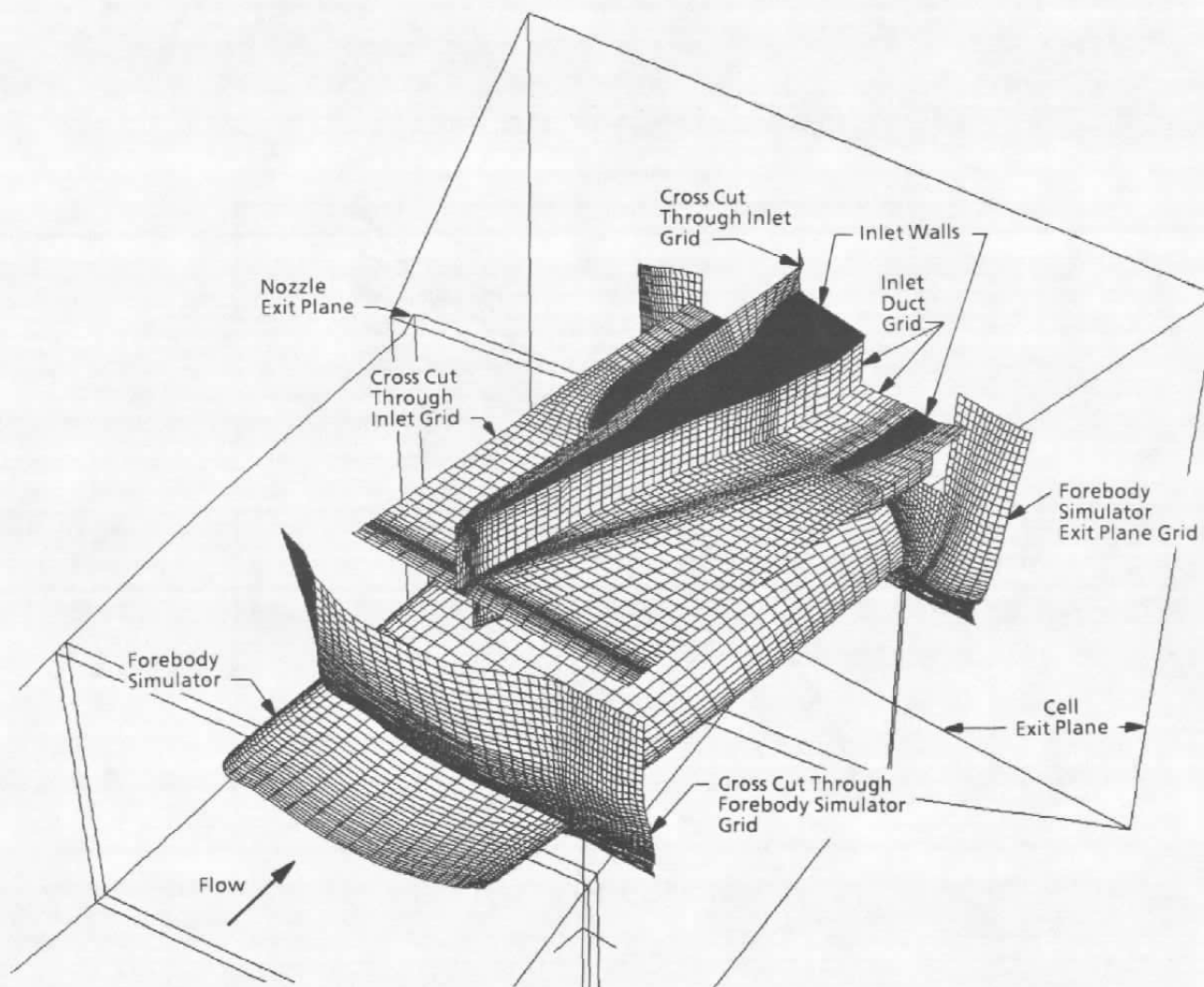and Cell Block Grids
by Forebody Simulator
and Inlet Blocks ⌐
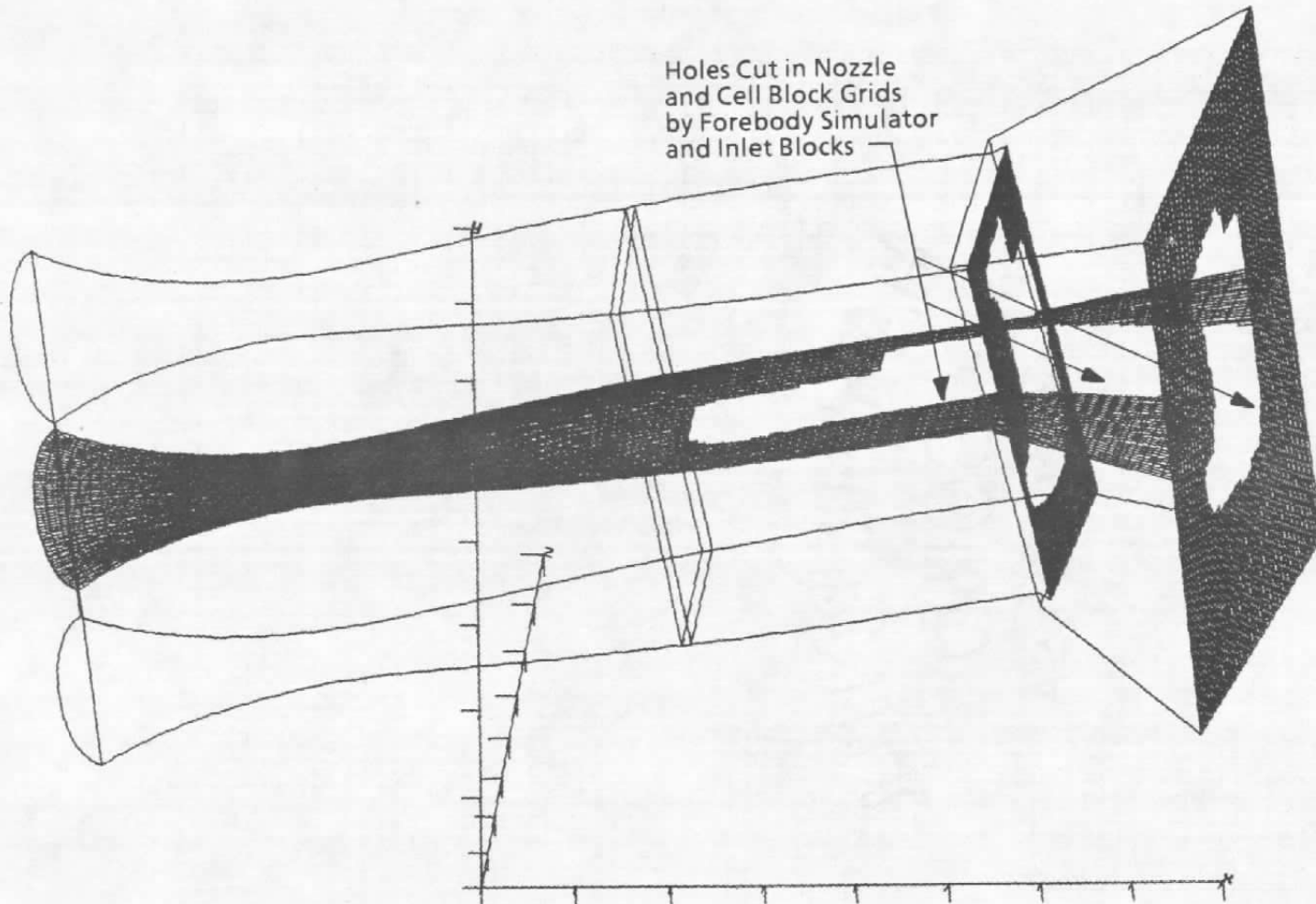
b. "Chimera" holes in nozzle and cell grids
Figure 11. Concluded.

Inlet
Mass Flow
Surface Grid

Forebody
Simulator

Inlet Wall

Cell Exit Grid
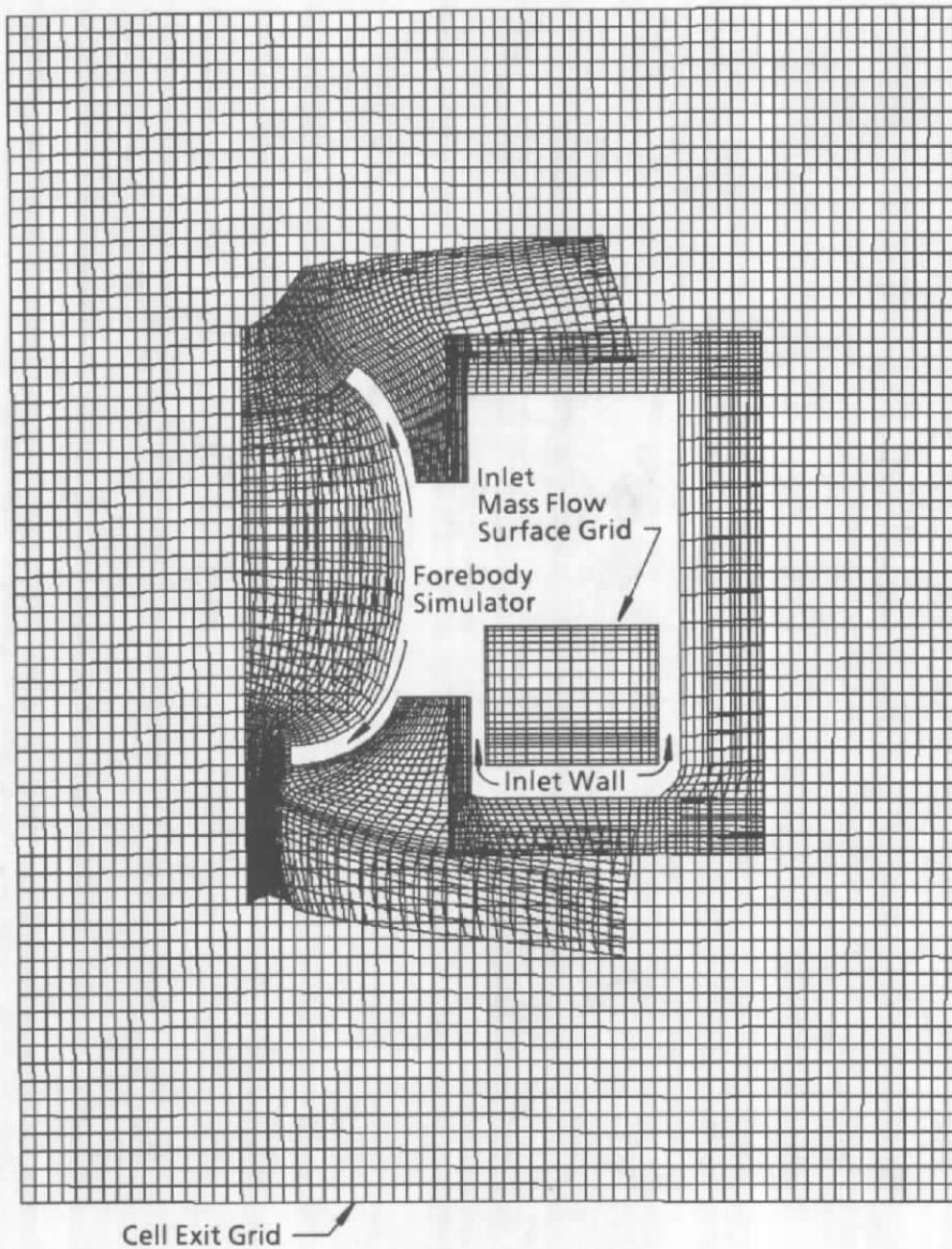
a. Exit plane grids
Figure 12. Selected supersonic grid plots.

Cross Cut
Through Inlet
Grid

Inlet Walls

Inlet
Duct
Grid

Nozzle
Exit Plane

Cross Cut
Through
Inlet Grid

Forebody
Simulator
Exit Plane Grid

Forebody
Simulator

Cell
Exit Plane

Cross Cut Through
Forebody Simulator
Grid

Flow

b. Forebody simulator and inlet block grids
Figure 12. Concluded.
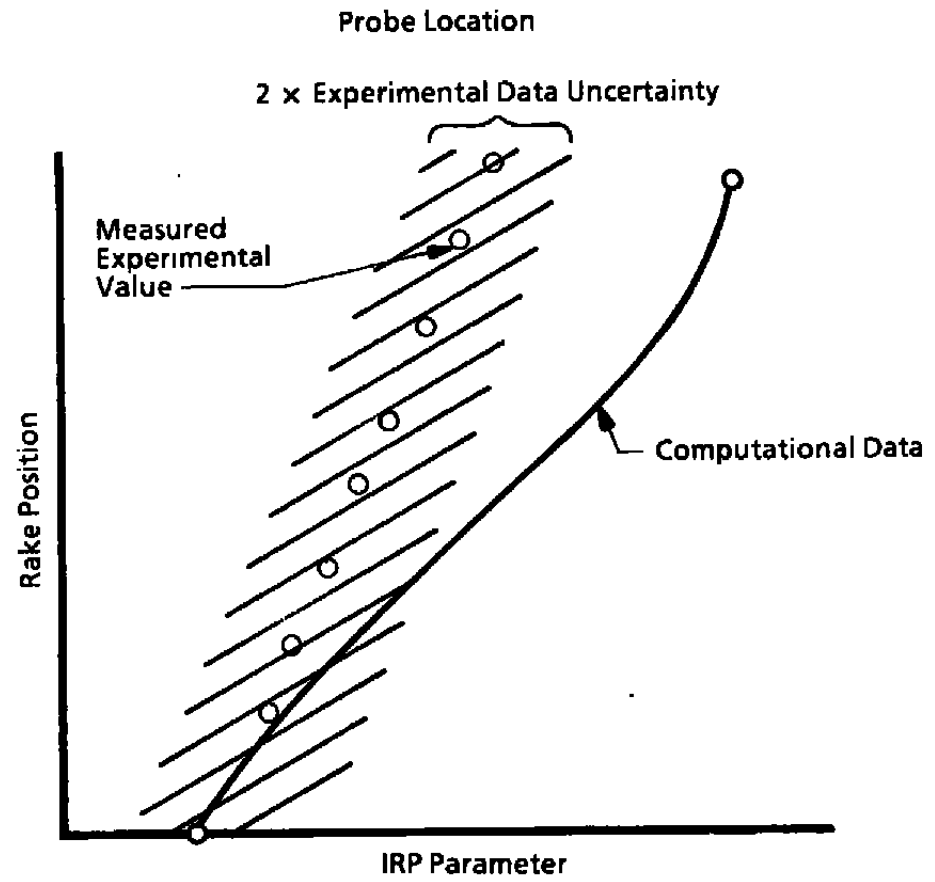
Figure 13. Comparison plot format.

○ FJ11 DP 177 to 186
▨ Experimental Band
● CFD Case 1

Test Conditions
Mach No. = 0.90
ALPHA = 30.00
BETA = 0
WC2 = 200.00

Inboard

Center

Outboard
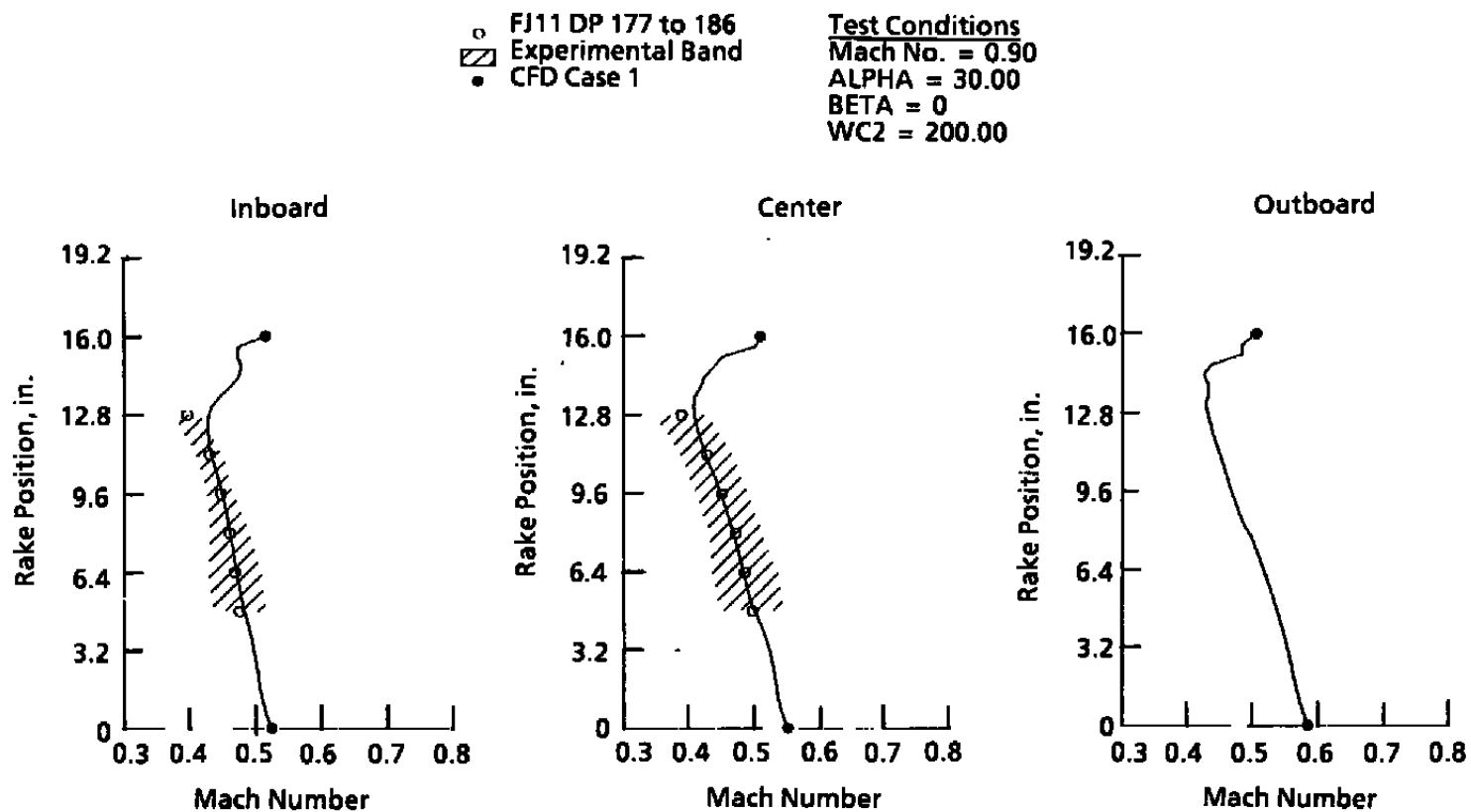
a. Mach number

Figure 14. Computation versus experiment — Mach = 0.9, ALPHA = 30.0, BETA = 0.
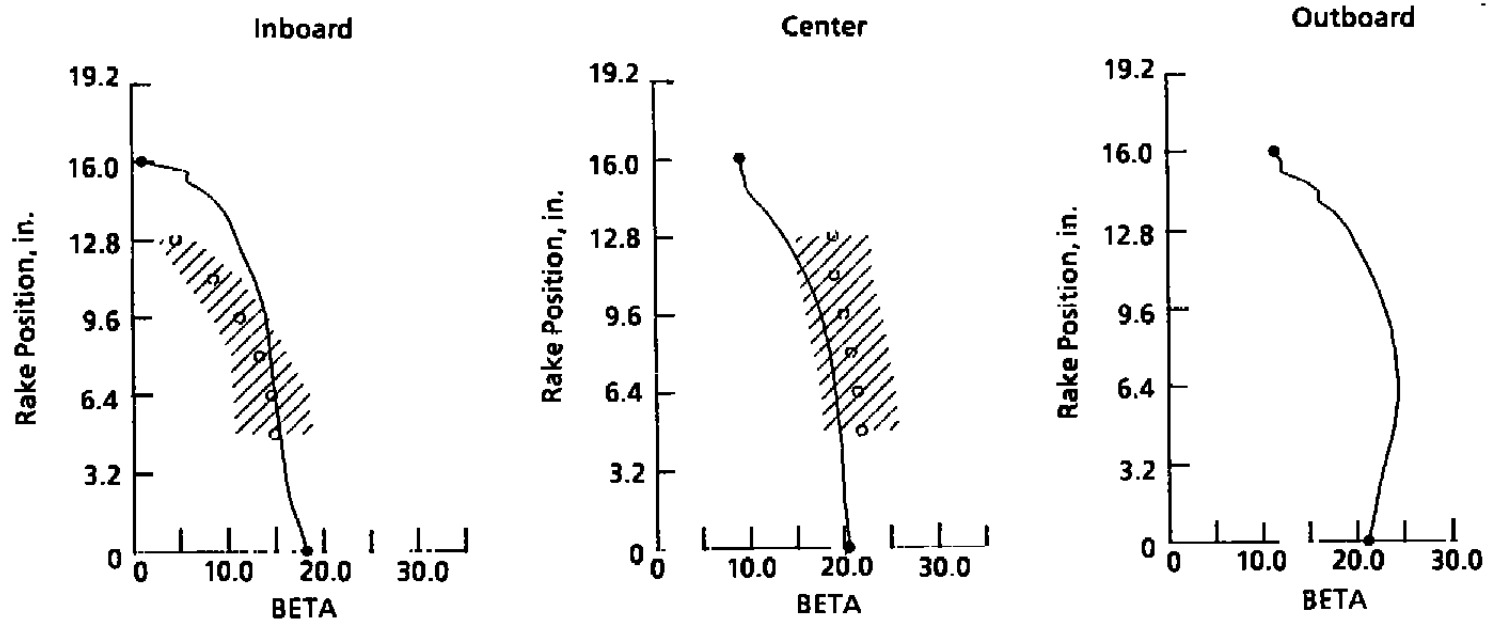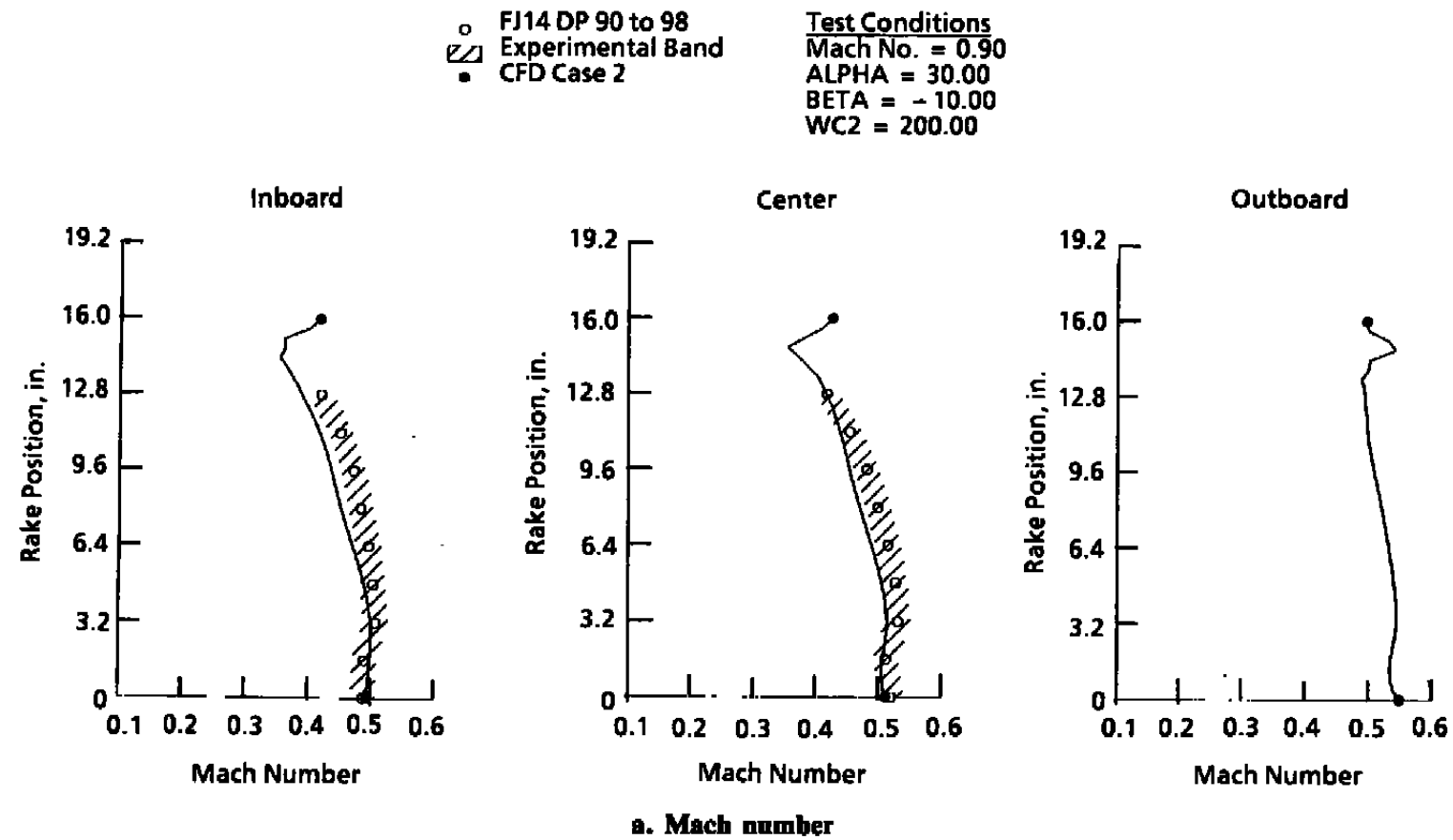
○ FJ11 DP 177 to 186
▨ Experimental Band
● CFD Case 1

Test Conditions
Mach No. = 0.90
ALPHA = 30.00
BETA = 0
WC2 = 200.00

Inboard

Center

Outboard

Rake Position, in.
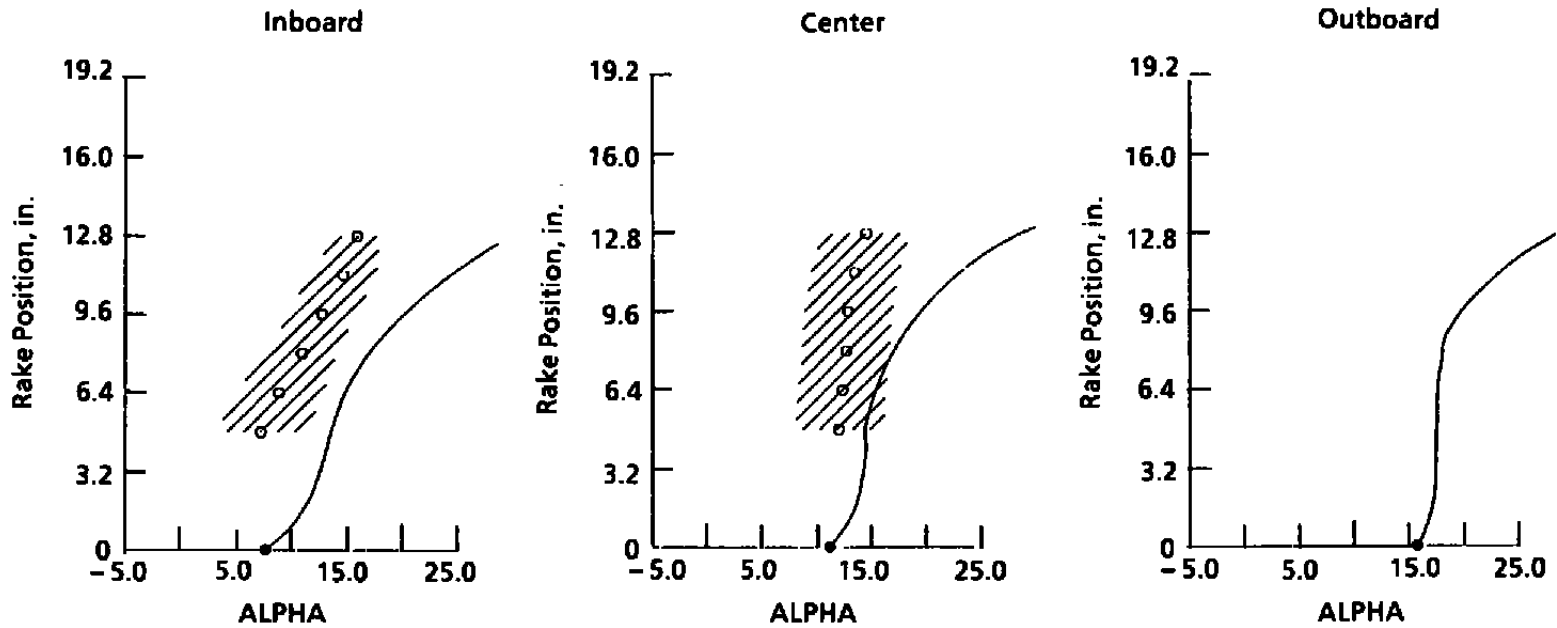
ALPHA

b. ALPHA
Figure 14. Continued.

o FJ11 DP 177 to 186   Test Conditions
⊡ Experimental Band   Mach No. = 0.90
• CFD Case 1   ALPHA = 30.00
                        BETA = 0
                        WC2 = 200.00

c. BETA
Figure 14. Concluded.

○   FJ14 DP 90 to 98   Test Conditions
▨   Experimental Band   Mach No. = 0.90
●   CFD Case 2   ALPHA = 30.00
                           BETA = − 10.00
                           WC2 = 200.00

a. Mach number

Figure 15. Computation versus experiment — Mach = 0.9, ALPHA = 30.0, BETA = −10.0.

o FJ14 DP 90 to 98
◪ Experimental Band
● CFD Case 2

Test Conditions
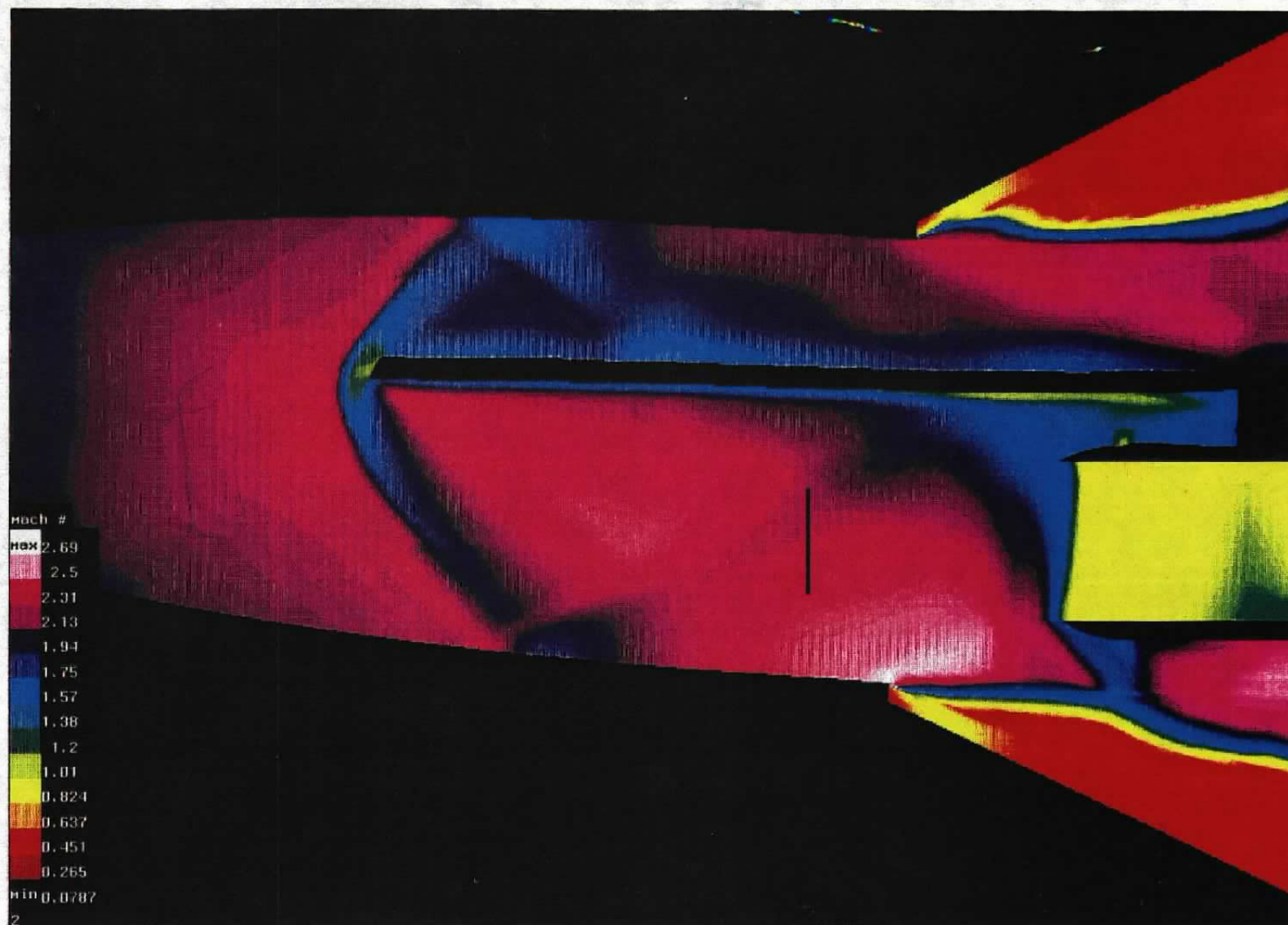Mach No. = 0.90
ALPHA = 30.00
BETA = −10.00
WC2 = 200.00

Inboard

Center

Outboard
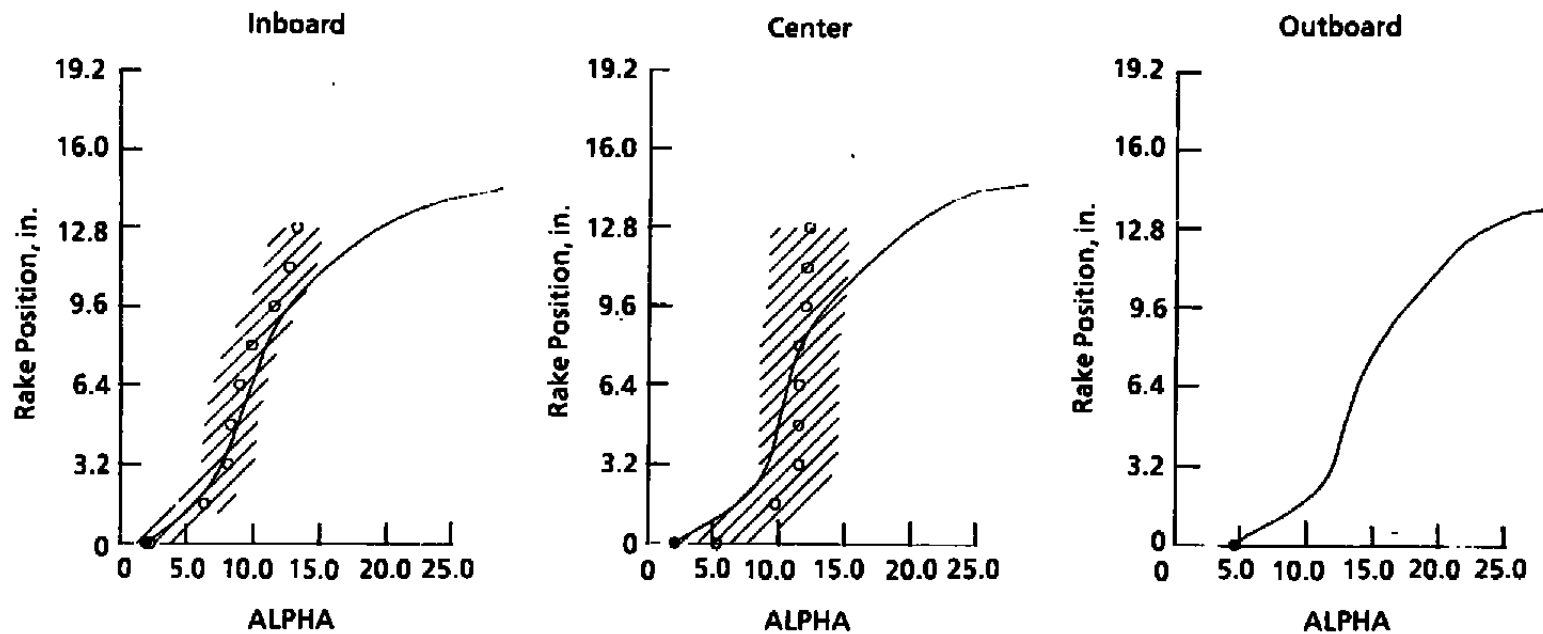
b. ALPHA
Figure 15. Continued.

o FJ14 DP 90 to 98
▨ Experimental Band
• CFD Case 2

Test Conditions
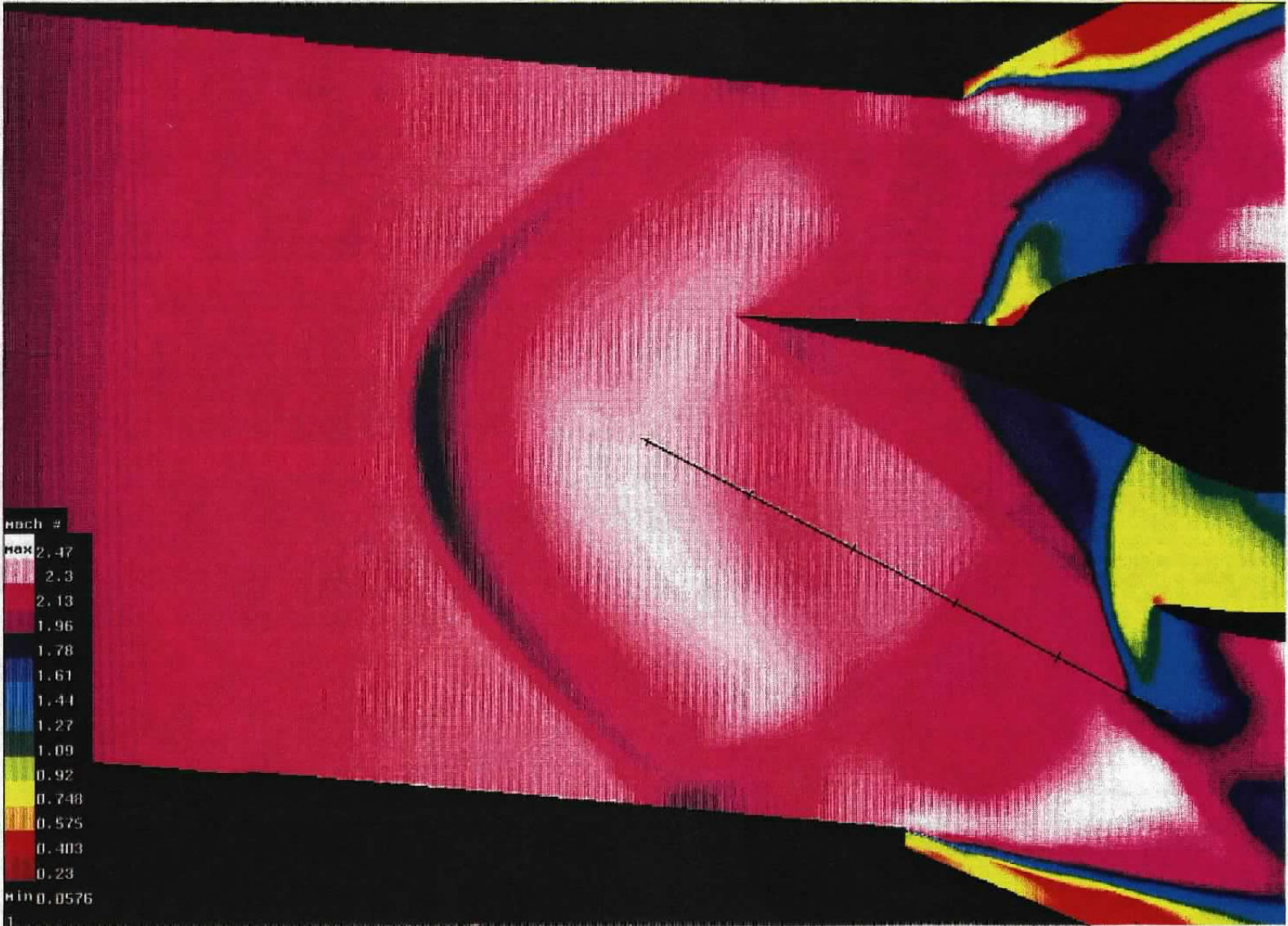Mach No. = 0.90
ALPHA = 30.00
BETA = − 10.00
WC2 = 200.00
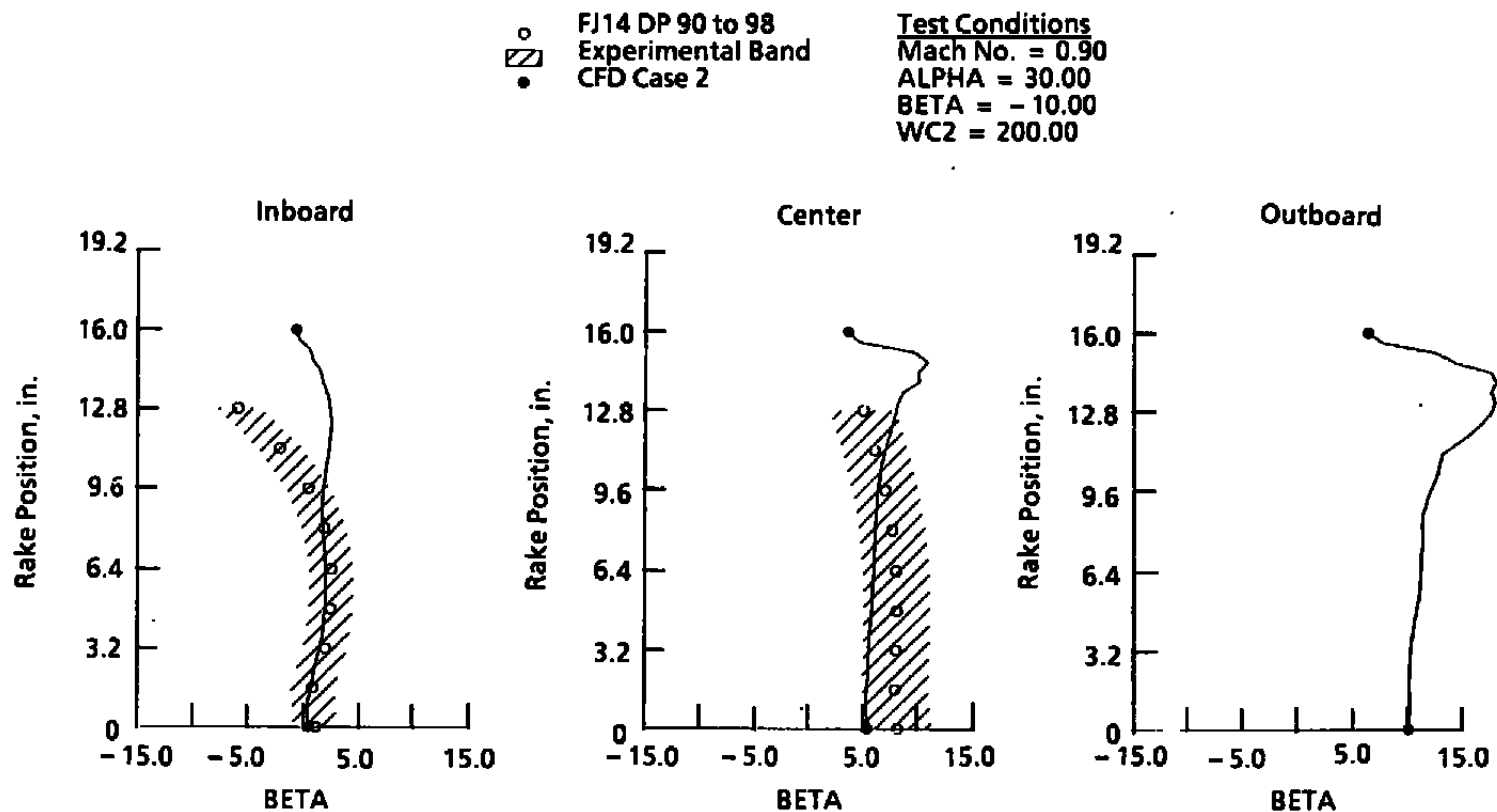
c. BETA
Figure 15. Concluded.

a. Plan view
Figure 16. Case 5 flow-field Mach contours.

b. Elevation view
Figure 16. Concluded.

Legend:
- ○ FJ42 DP 26 to 33
- ▨ Experimental Band
- ● CFD Case 3

Test Conditions
Mach No. = 2.20
ALPHA = 12.00
BETA = 3.00
WC2 = 188.00

Inboard

Center

Outboard
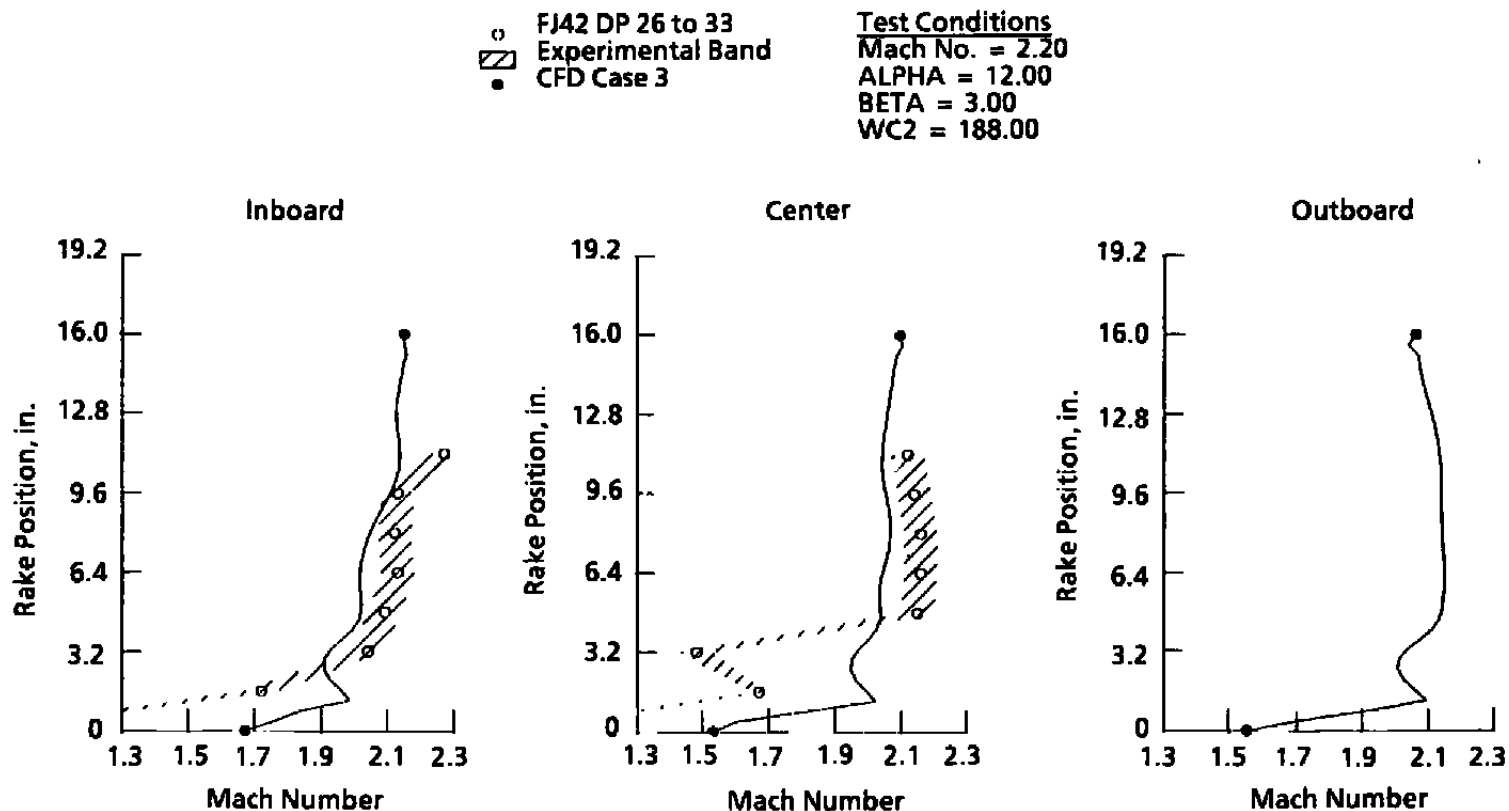
a. Mach number
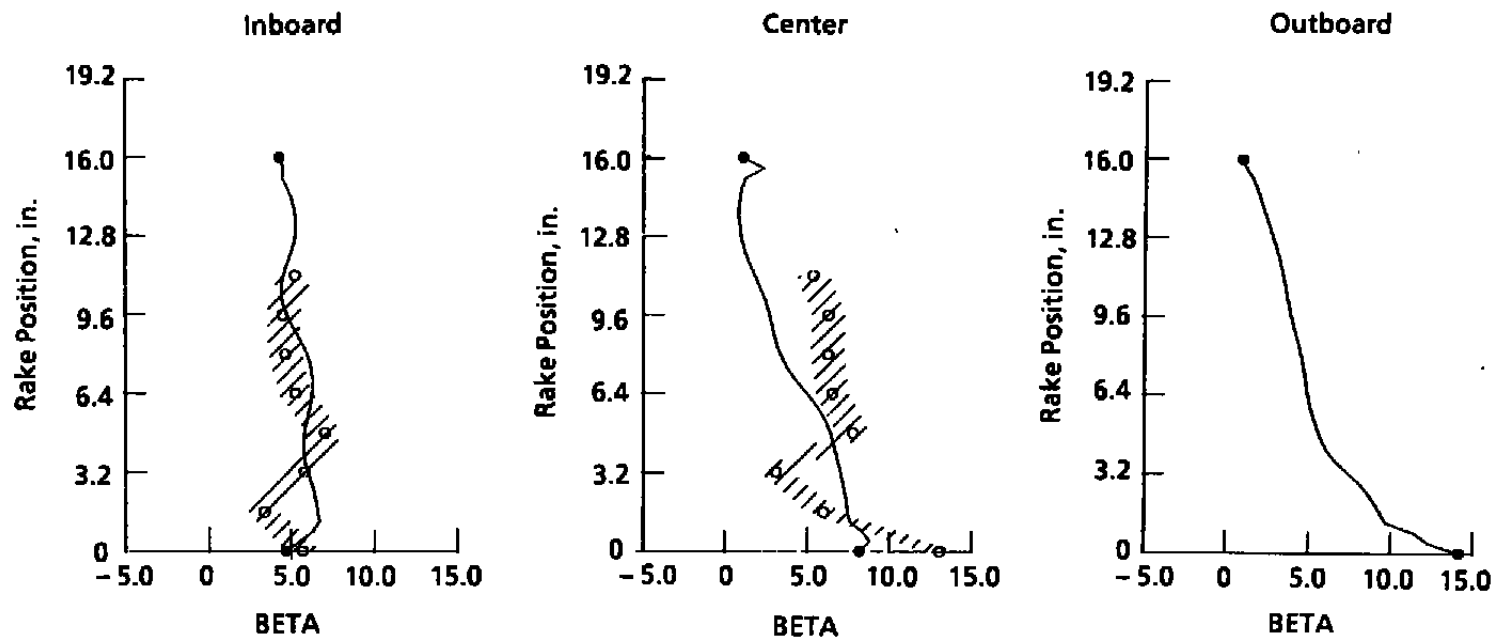
Figure 17. Computation versus experiment — Mach = 2.2, ALPHA = 12.0, BETA = 3.0.
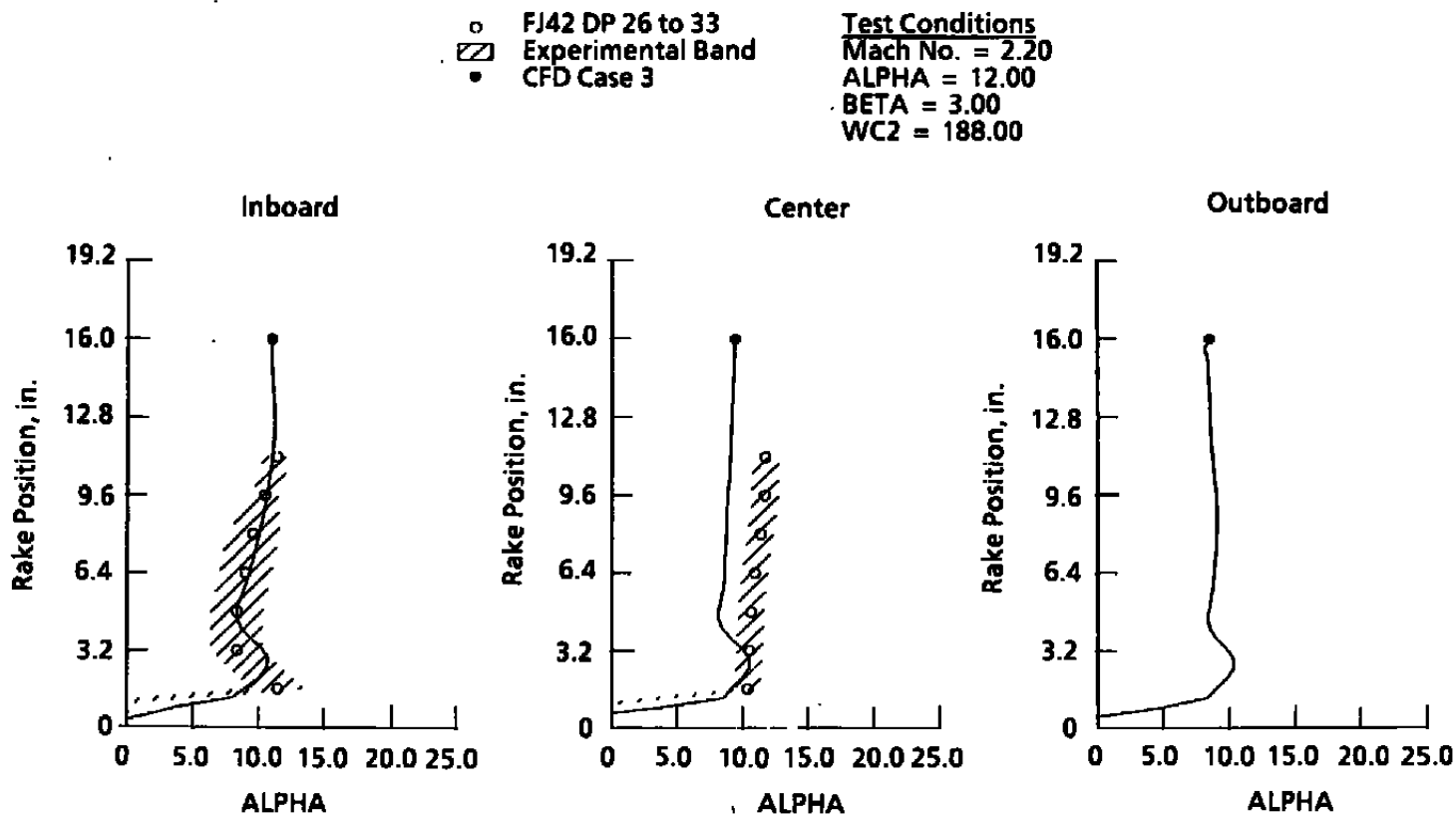
b. ALPHA

Figure 17. Continued.

o   FJ42 DP 26 to 33   Test Conditions
⊠ Experimental Band   Mach No. = 2.20
●   CFD Case 3   ALPHA = 12.00
                           BETA = 3.00
                           WC2 = 188.00

Inboard   Center   Outboard

c. BETA
Figure 17. Concluded.

a. Mach number

Figure 18. Computation versus experiment — Mach = 2.2, ALPHA = 12.0, BETA = 0.

67

○ FJ42 DP 26 to 33 ·
▱ Experimental Band
● CFD Case 4

Test Conditions
Mach No. = 2.20
ALPHA = 12.00
BETA = 0
WC2 = 188.00

Inboard

Center

Outboard
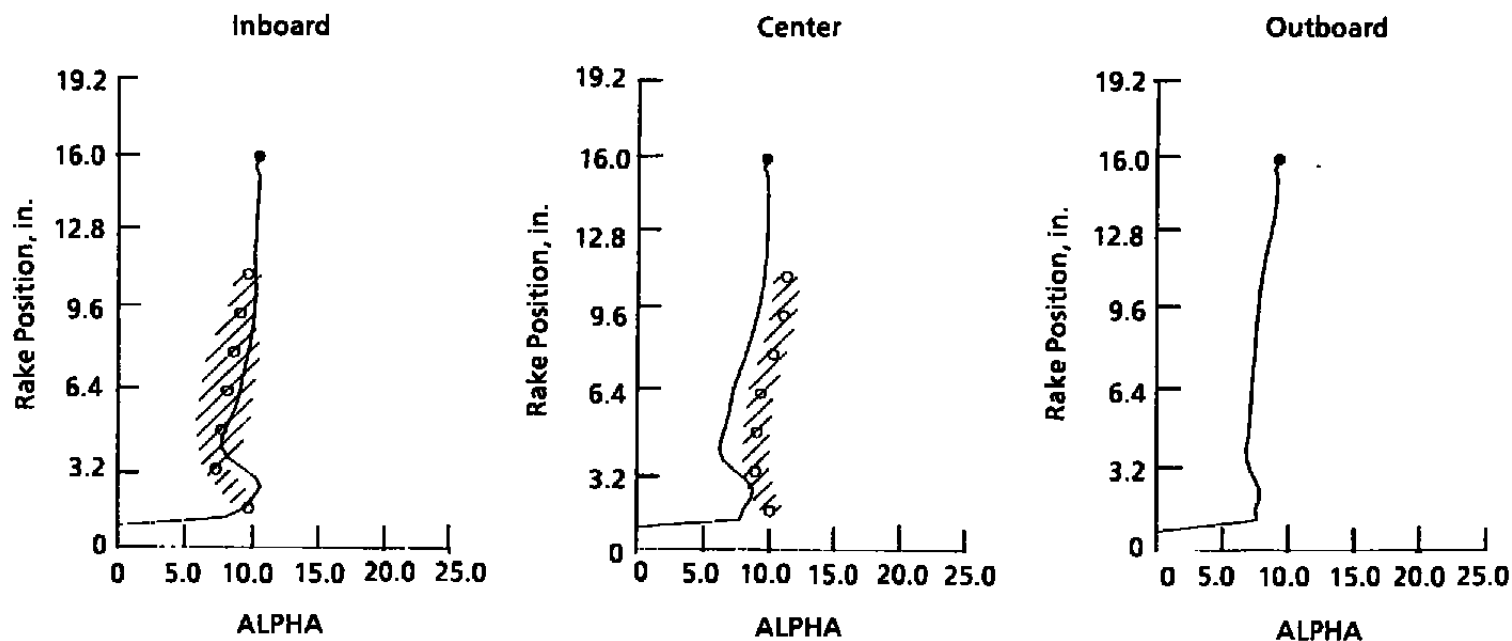
b. ALPHA
Figure 18. Continued.

o   FJ42 DP 26 to 33
▨   Experimental Band
•   CFD Case 4

<u>Test Conditions</u>
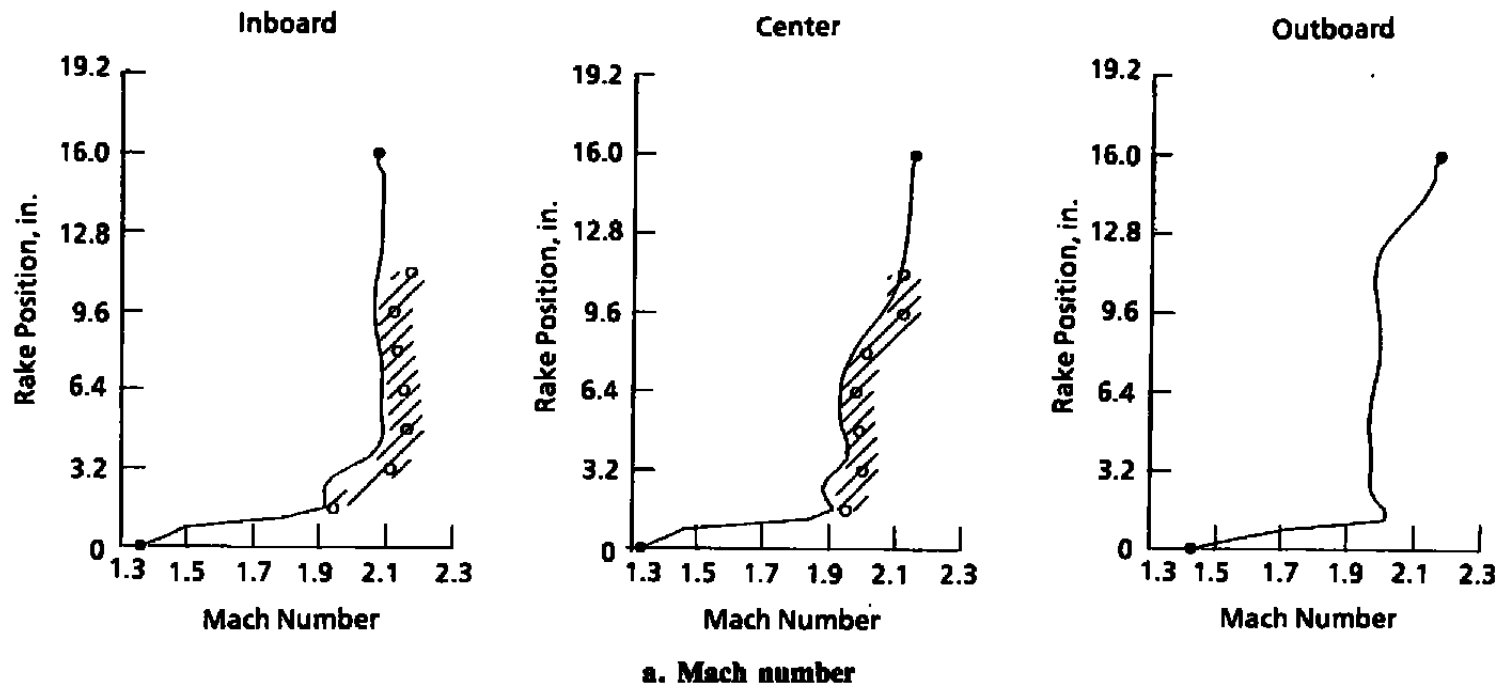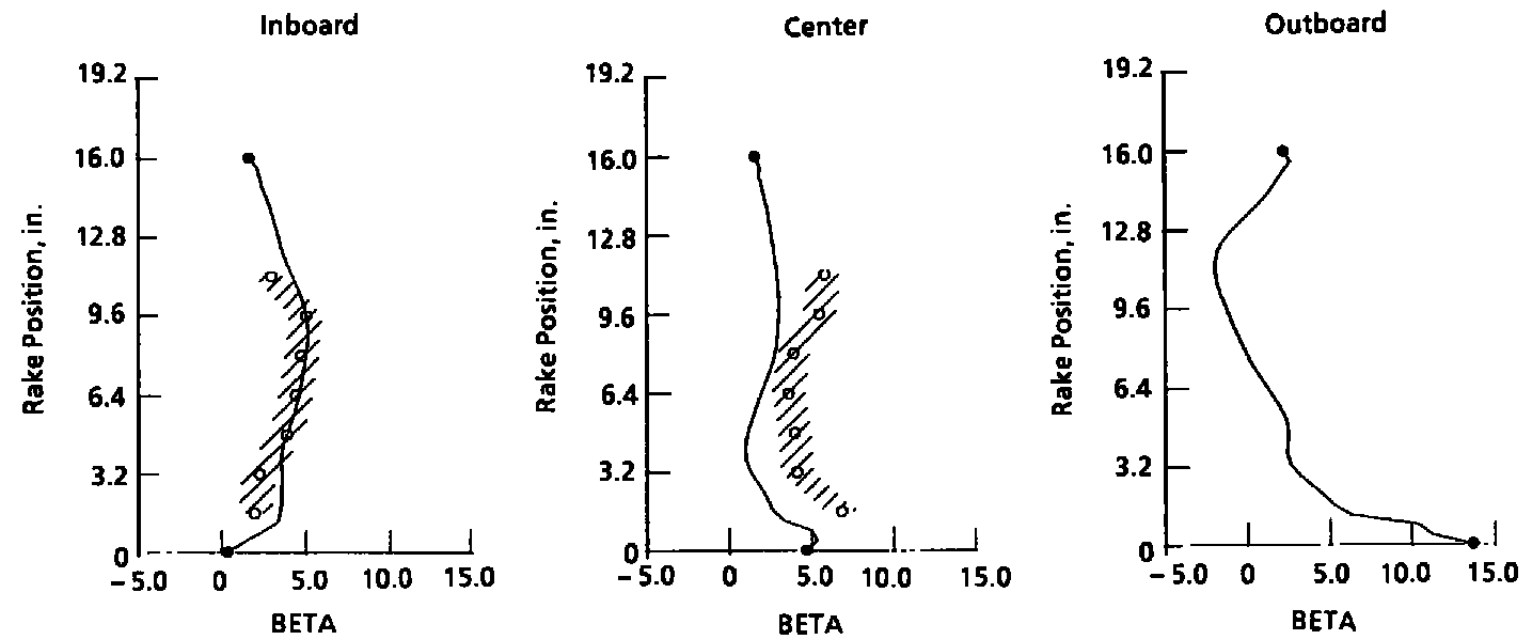Mach No. = 2.20
ALPHA = 12.00
BETA = 0
WC2 = 188.00

Inboard

Center

Outboard

c. BETA
Figure 18. Concluded.

○ FJ43 DP 17 to 23   <u>Test Conditions</u>
▨ Experimental Band   Mach No. = 2.20
● CFD Case 5   ALPHA = 0
   BETA = 0
   WC2 = 188.00
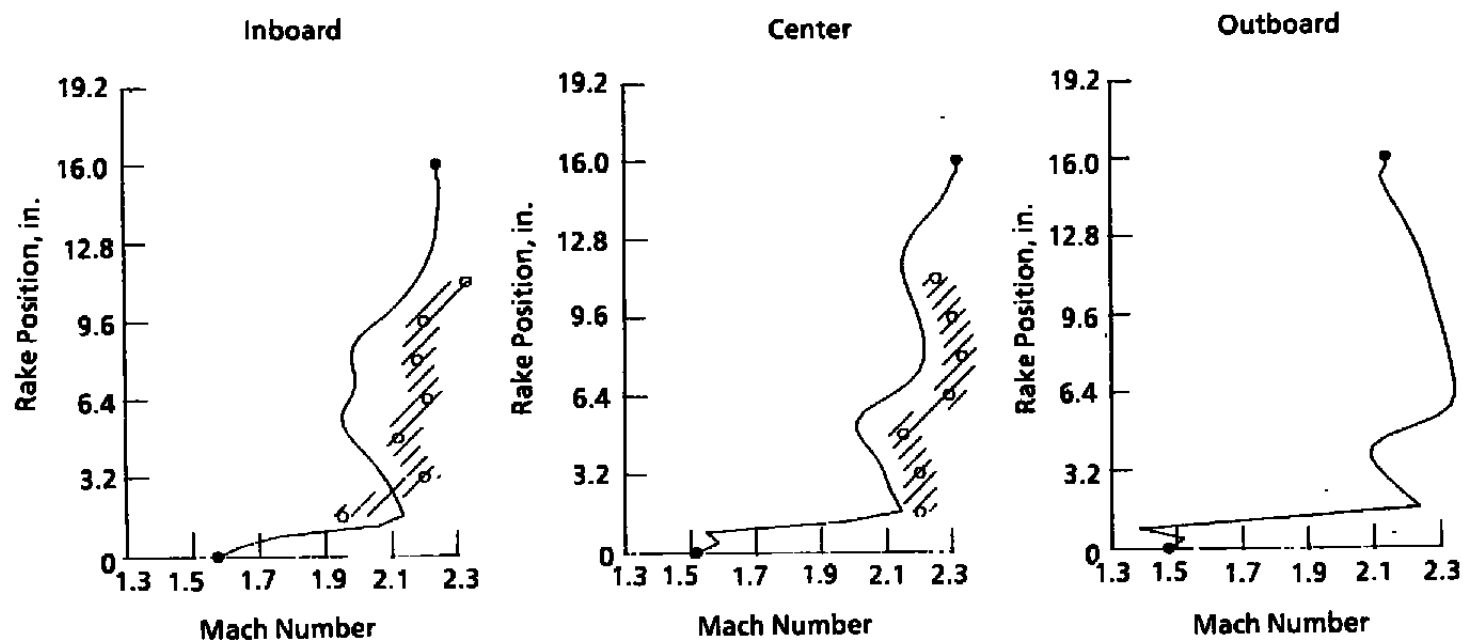
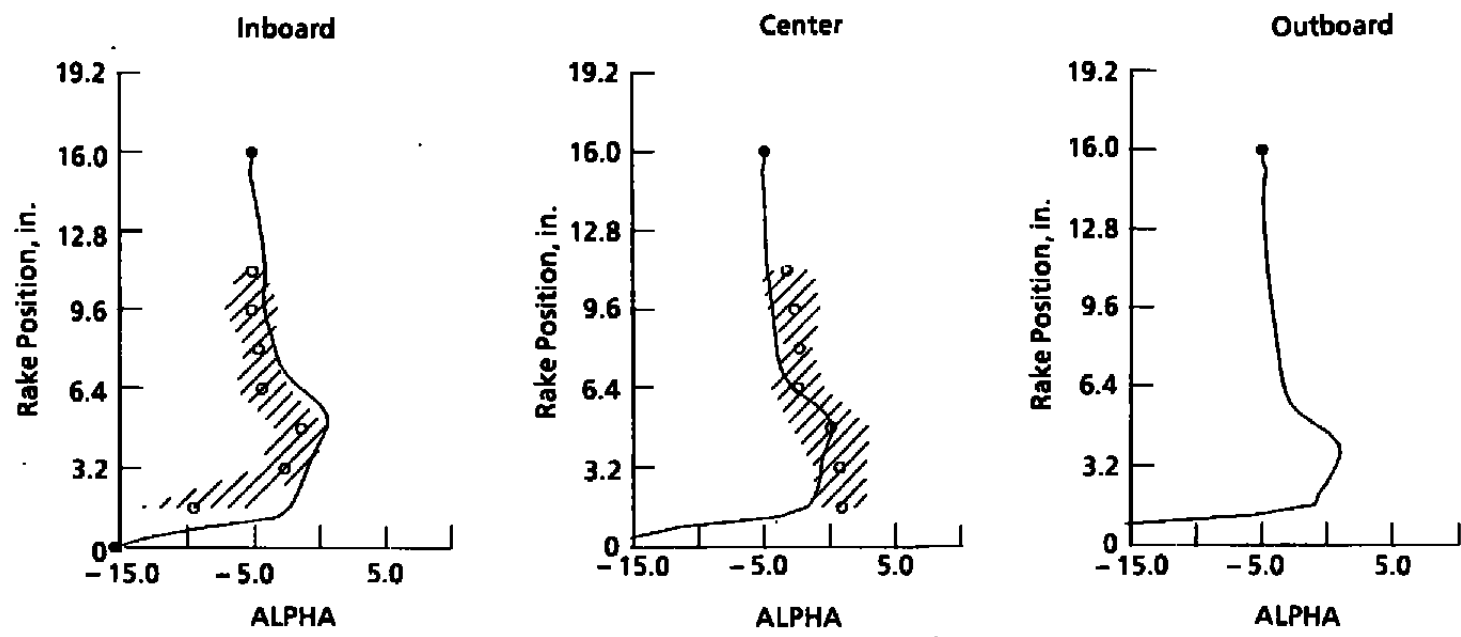

a. Mach number

Figure 19. Computation versus experiment — Mach = 2.2, ALPHA = 0, BETA = 0.

o FJ42 DP 26 to 33
▧ Experimental Band
● CFD Case 5

<u>Test Conditions</u>
Mach No. = 2.20
ALPHA = 0
BETA = 0
WC2 = 188.00

Inboard

Center

Outboard

b. ALPHA
Figure 19. Continued.

o   FJ42 DP 26 to 33
ⵠⵉ Experimental Band
●   CFD Case 5

Test Conditions
Mach No. = 2.20
ALPHA = 0
BETA = 0
WC2 = 188.00

Inboard

Center

Outboard
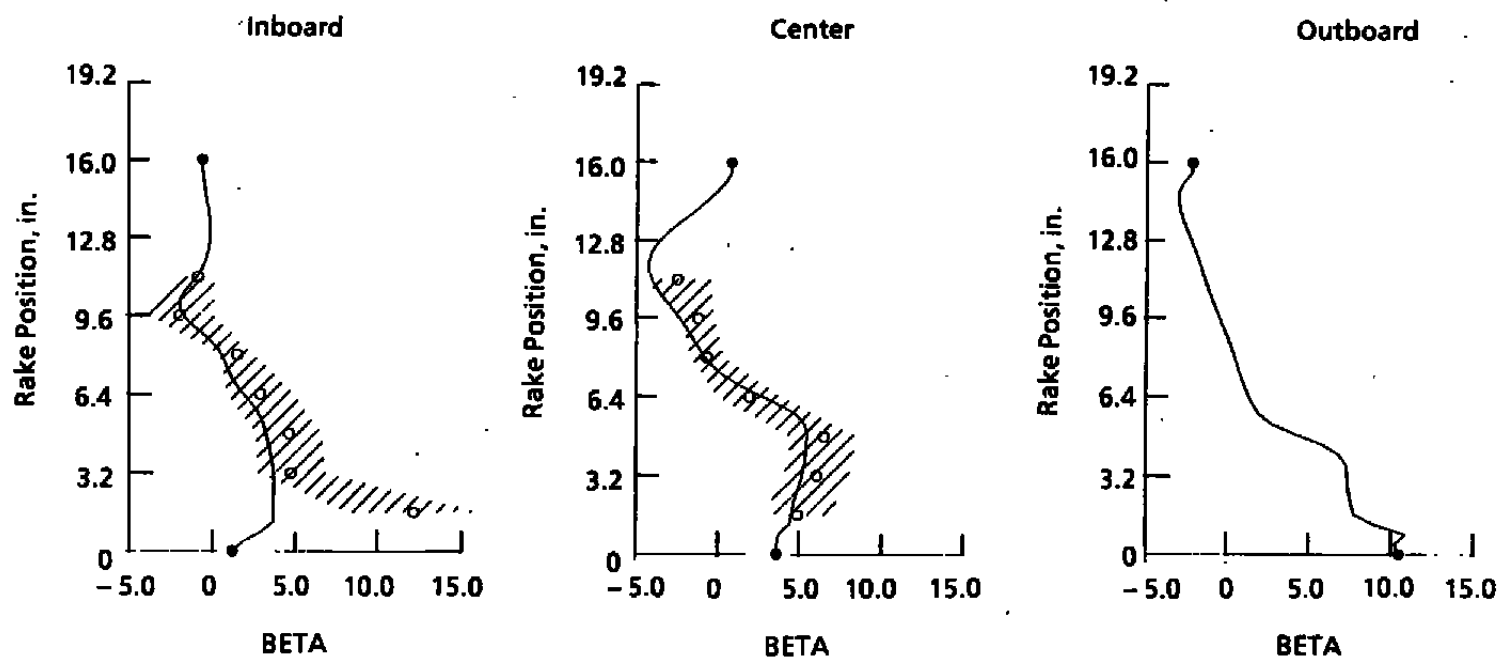
c. BETA
Figure 19. Concluded.

Table 1. Free-Jet Test Matrix

Subsonic

Corrected Mass Flow

Mach = 0.3, 0.6, 0.9
$WC2_1$ = 260 lbm/sec
$WC2_2$ = 230 lbm/sec
$WC2_3$ = 200 lbm/sec

Supersonic

Mach = 2.2
$WC2_1$ = 210   188 lbm/sec
$WC2_2$ = 170   170 lbm/sec
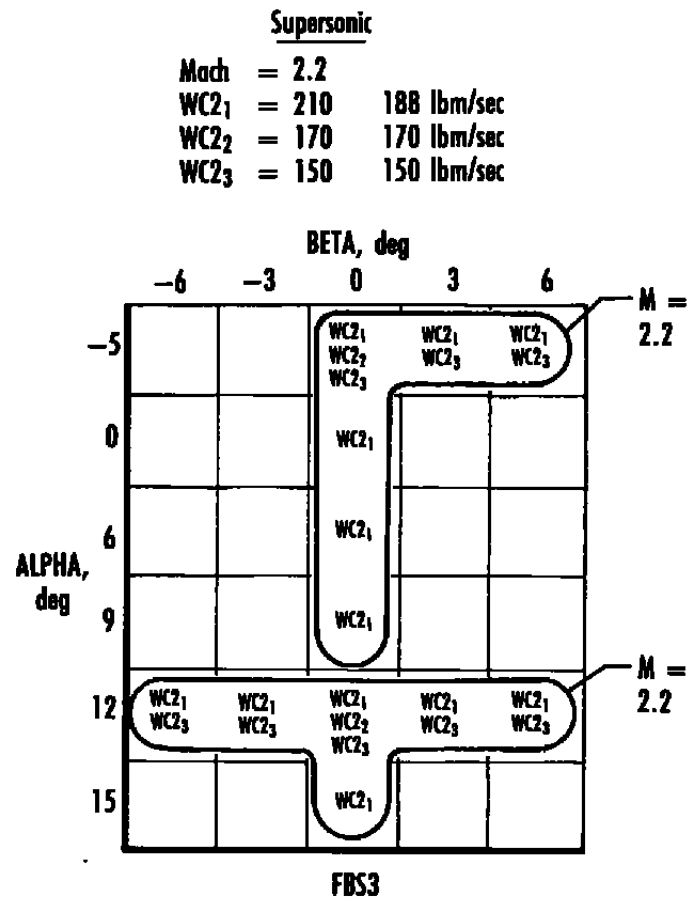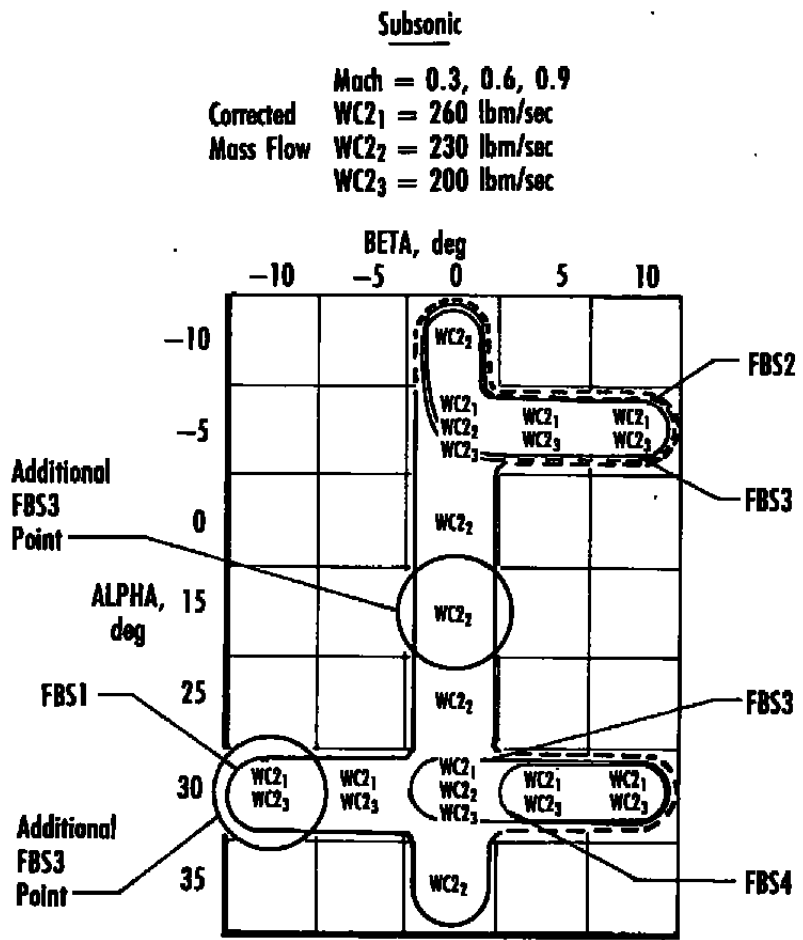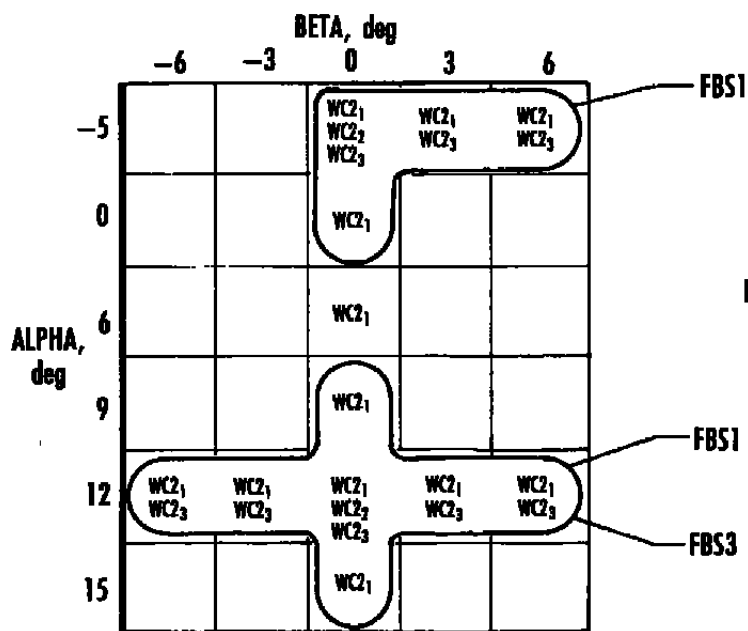$WC2_3$ = 150   150 lbm/sec

Table 2. Additional Free-Jet Test Cases

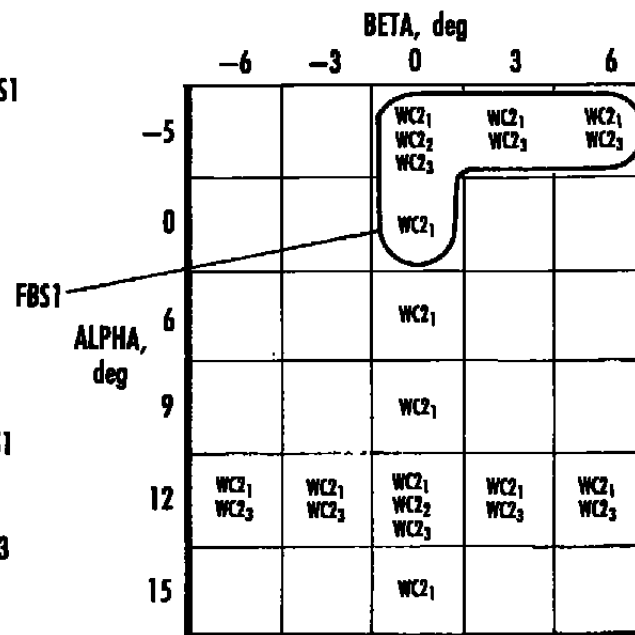### Free-Jet Test Matrix — Supersonic

Mach 1.6

$WC2_1 = 210$ lbm/sec
$WC2_2 = 170$ lbm/sec
$WC2_3 = 150$ lbm/sec

Corrected
Mass Flow

Mach 2.2

$WC2_1 = 188$ lbm/sec
$WC2_2 = 170$ lbm/sec
$WC2_3 = 150$ lbm/sec

Table 3. Simulated Free-Stream Conditions

Case	Mach	ALPHA, deg	BETA, deg	FBS	WC2
1	0.9	30.0	0	1	200.0 lbm/sec
2	0.9	30.0	−10	1	200.0 lbm/sec
3	2.2	12.0	3.0	3	188.0 lbm/sec
4	2.2	12.0	0	3	188.0 lbm/sec
5	2.2	0	0	3	188.0 lbm/sec

Table 4. Summary of Differences Between Experimental and CFD IRP Data

		Case 1	Case 2	Case 3	Case 4	Case 5	Parameter Average
MACH*	Minimum	0.0005	0.0016	0.0234	0.101	0.0919	
	Maximum	0.0329	0.0361	0.485	0.131	0.235	
	Number of Points	12	18	14	14	14	
	Average	0.0068	0.0196	0.148	0.0612	0.142	0.0743
ALPHAI	Minimum	2.40	0.185	0.0008	0.279	0.0616	
	Maximum	14.1	7.52	18.3	2.48	6.99	
	Number of Points	12	18	16	14	14	
	Average	7.42	2.15	3.09	1.44	1.86	3.02 deg
BETAI	Minimum	0.355	0.0967	0.209	0.0182	0.0936	
	Maximum	6.44	8.37	4.88	4.09	8.64	
	Number of Points	12	18	16	14	14	
	Average	2.77	1.95	2.00	1.60	1.37	1.92 deg

*MACHI Prediction Accuracy Is Determined Only Upstream of the Point Where the Cowl and Ramp Shocks Cross the IRP.

NOMENCLATURE

ALPHA	Wind tunnel or flight angle-of-attack, deg
ALPHAI	Local flow angle-of-attack measured at the IRP and referenced to the aircraft fixed axis system, deg
ALPHAP	Local flow angle-of-attack measured at the IRP and referenced to the probe fixed axis system, deg
BETA	Wind tunnel or flight angle-of-sideslip, deg
BETAI	Local flow angle-of-sideslip measured at the IRP and referenced to the aircraft fixed axis system, deg
BETAP	Local flow angle-of-sideslip measured at the IRP and referenced to the probe fixed axis system, deg
IRP	Inlet reference plane
MACH	Wind tunnel or flight Mach number
MACHI	Local flow Mach number measured at the IRP
RANGLE	Probe rake mount angle relative to aircraft fixed, deg (Fig. 3)
u,v,w	Components of IRP total velocity vector
V	IRP total velocity vector
WC2	Full-scale engine face airflow rate corrected to standard-day sea-level conditions, lbm/sec
x,y,z	Probe fixed axis system (Fig. 3)
x′,y′,z′	Aircraft fixed axis system